

Defining eccentricity for spin-precessing binaries

Md Arif Shaikh ^{1,2}, Vijay Varma ³, Antoni Ramos-Buades ⁴, Harald P. Pfeiffer ⁵, Michael Boyle ⁶, Lawrence E. Kidder ⁶, and Mark A. Scheel ⁷

¹ Department of Physics, Vivekananda Satavarshiki Mahavidyalaya (affiliated to Vidyasagar University), Manikpara 721513, West Bengal, India

² Department of Physics and Astronomy, Seoul National University, Seoul 08826, Korea

³ Department of Mathematics, Center for Scientific Computing and Data Science Research, University of Massachusetts, Dartmouth, MA 02747, USA

⁴ Departament de Física, Universitat de les Illes Balears, IAC3 – IEEC, Crta. Valldemossa km 7.5, E-07122 Palma, Spain

⁵ Max Planck Institute for Gravitational Physics (Albert Einstein Institute), D-14476 Potsdam, Germany

⁶ Cornell Center for Astrophysics and Planetary Science, Cornell University, Ithaca, New York 14853, USA

⁷ Theoretical Astrophysics 350-17, California Institute of Technology, Pasadena, CA 91125, USA

E-mail: arifshaikh.astro@gmail.com

Abstract. Standardizing the definition of eccentricity is necessary for unambiguous inference of the orbital eccentricity of compact binaries from gravitational wave observations. In previous works, we proposed a definition of eccentricity for systems without spin-precession that relies solely on the gravitational waveform, is applicable to any waveform model, and has the correct Newtonian limit. In this work, we extend this definition to spin-precessing systems. This simple yet effective extension relies on first transforming the waveform from the inertial frame to the coprecessing frame, and then adopting an amplitude and a phase with reduced spin-induced effects. Our method includes a robust procedure for filtering out spin-induced modulations, which become non-negligible in the small eccentricity and large spin-precession regime. Finally, we apply our method to a set of Numerical Relativity and Effective One Body waveforms to showcase its robustness for generic eccentric spin-precessing binaries. We make our method public via Python implementation in `gw_eccentricity`.

Keywords: Gravitational Waves, Compact Binary Coalescences, Eccentricity, Numerical Relativity, Black Holes

1. Introduction

The ground-based network of gravitational wave (GW) detectors, LIGO-Virgo-KAGRA (LVK) [1–3], has observed ~ 90 compact binary coalescences (CBCs) during the first three observation runs (O1, O2, and O3) [4–7]. The increasing number of detected GW signals can enable us to address one of the key scientific questions in GW astronomy—how do these binaries form in nature? Two main formation channels are generally considered for compact binaries: the first is the isolated formation channel, where the binary evolves without interactions with any third object [8, 9]. The second is the dynamical formation channel, where the binary can undergo frequent interactions with other objects in a dense stellar environment, such as a globular cluster [10, 11] or near an active galactic nucleus [12–14].

Eccentricity and the spins of black holes provide valuable clues about the formation history of a binary. Due to the loss of energy and angular momentum via GW emission, the orbital eccentricity of a binary decays over time as the system inspirals [15, 16]. As a result, for binaries evolving in isolation, the orbit becomes circularized by the time their GWs enter the sensitivity band of ground-based GW detectors. On the other hand, in dense stellar environments, dynamical interactions can harden the binary, leading to a merger with non-negligible eccentricity [10, 11]. Similarly, eccentricity can be amplified due to binary-single interactions in an active galactic nucleus (AGN) disk [12–14] or via the Kozai-Lidov mechanism in the presence of a third object near the binary [17–20].

Similar to eccentricity, the formation history also influences the spins of black holes. In the isolated formation scenario, the spins of black holes are aligned with respect to the orbital angular momentum of the binary [8, 9]. On the other hand, in a dynamical environment, random interactions can produce black hole spins with arbitrary orientations [8]. When the spins are tilted relative to the orbital angular momentum, spin-spin and spin-orbit interactions cause the orbital plane to precess around the total angular momentum of the system [21, 22]. This has a direct imprint on the amplitude and frequency of the GW signal, and can therefore be used to infer the black hole spins from GW observations as long as gravitational waveform models accurately capture the effects of spin-precession.

Similarly, accurately modeling the effects of eccentricity is necessary to reliably measure eccentricity from GW observations. Inclusion of eccentricity in waveform models is essential not only to avoid systematic bias in the parameters inferred from GWs data [23–30], but also to avoid false violation of General Relativity (GR) in tests of GR using GWs [31–33]. Accurate quasicircular waveform models that capture spin-precession have been developed [34–53]. Similarly, accurate eccentric aligned-spin waveform models have also been developed [24, 54–70]. However, to reliably extract the eccentricity and spins of black holes from GWs, accurate waveform models that incorporate both eccentricity and spin-precession effects are required.

Ongoing efforts aim to develop waveform models that include both effects, for example, using Numerical Relativity (NR) simulations [71, 72], Post-Newtonian (PN) theory [73–77] and the effective one-body (EOB) formalism [78–80]. Several works have already placed constraints on eccentricity of the observed GW events [71, 81–86], but they require further

refinement using improved waveform models that capture the full physics of eccentricity and spin-precession (see [87] for a first step in this direction).

A key challenge in constraining eccentricity from GW observations is that eccentricity is not uniquely defined in GR. In fact, different waveform models use different internal definitions of eccentricity, which can lead to ambiguity in the inferred orbital eccentricity. Several works have made efforts to standardize the definition of eccentricity [88–94]. References [89, 90] proposed a standardized definition of eccentricity that relies only on the gravitational waveform, can be applied to any waveform model, and has the correct Newtonian limit. However, the definition proposed in [89, 90] assumes that the black hole spins are either aligned or anti-aligned with the orbital angular momentum, that is, the orbital plane remains fixed. In this work, we relax this assumption and extend the definition of eccentricity to systems with spin-precession, where the black hole spins may be tilted with respect to the orbital angular momentum.

We generalize the standardized definition of eccentricity by using the waveform in the coprecessing frame and using variables with reduced spin-induced effects. We show that our generalized definition can be robustly applied to waveforms from different origins and broad range of eccentricities. The robustness of our eccentricity estimation is achieved through two additional improvements: an adaptive interpolation method based on rational function approximation, and an additional processing step for removing residual spin-induced oscillations in the amplitude and frequency using low-pass filtering. Additionally, we briefly explore the influence of the gravitational-wave memory effect on eccentricity measurements, and demonstrate that subtracting the memory contribution leads to more consistent and reliable eccentricity estimates.

The rest of the paper is organized as follows: In section 2, we discuss the methods for generalizing the definition of eccentricity, and provide a summary of the steps required to measure eccentricity for spin-precessing systems. In section 3, we apply the generalized definition across different waveform models and eccentricities to check the robustness of our method, and conclude in section 4.

2. Generalizing the definition of eccentricity to spin-precessing binaries

2.1. Notation and conventions

GW emitted by a compact binary can be represented as a complex combination \hat{h} of its two polarizations, h_+ (plus) and h_\times (cross): $\hat{h} \equiv h_+ - ih_\times$. The complex waveform \hat{h} can be decomposed into a sum of spin-weighted spherical harmonic modes $\hat{h}_{\ell,m}$ such that the waveform along any direction (ι, φ_0) in the binary’s source frame can be expressed as

$$\hat{h}(t, \iota, \varphi_0) = \sum_{\ell=2}^{\ell=\infty} \sum_{m=-\ell}^{m=\ell} \hat{h}_{\ell,m}(t) {}_{-2}Y_{\ell,m}(\iota, \varphi_0), \quad (1)$$

where ι and φ_0 are the polar and the azimuthal angles, respectively, on the sky in the source frame of the binary. ${}_{-2}Y_{\ell,m}$ are the spin=-2 weighted spherical harmonics.

For a given complex mode $h_{\ell,m}$, we can define corresponding amplitude $A_{\ell,m}$, phase $\phi_{\ell,m}$ and the angular frequency $\omega_{\ell,m}$ as

$$h_{\ell,m} = A_{\ell,m} e^{-i\phi_{\ell,m}}, \quad (2)$$

$$\omega_{\ell,m} = \frac{d\phi_{\ell,m}}{dt}. \quad (3)$$

For a binary system on a generic bound orbit, the waveform modes $h_{\ell,m}(t)$ depend on the component masses (m_1 and m_2 , with $m_1 \geq m_2$), six spin components (three for each compact object), two eccentricity parameters (eccentricity and mean anomaly), and the luminosity distance. The eccentricity parameters and black hole spins (for spin-precessing binaries) evolve over time, and, therefore these quantities should be defined at a fixed reference time (or frequency). Unless explicitly specified, we work with $h_{\ell,m}(t)$ at future null infinity scaled to unit total mass and luminosity distance. Thus, the system at a given reference time (or frequency) is characterized by 9 parameters — the mass ratio ($q = m_1/m_2$), the dimensionless spin vectors (χ_1, χ_2), and the two eccentricity parameters. Finally, it is convenient to define an effective spin-precession parameter χ_p that approximately quantifies the amount of spin-precession in a system [95]

$$\chi_p = \max\left(\chi_1 \sin \theta_1, \frac{4q+3}{4+3q} q \chi_2 \sin \theta_2\right), \quad (4)$$

where χ_i is the component spin magnitude with $i = 1, 2$ and θ_i is the component spin tilt relative to the orbital angular momentum.

Throughout the paper, we shift the time array of the waveform such that $t = 0$ occurs at the peak of the waveform amplitude defined in equation (5) of [42] \ddagger . Eccentricity, mean anomaly, and black hole spins (for spin-precessing binaries) are presented at a fixed time before the peak.

2.2. Effect of eccentricity and spin-precession on the waveform

The GW modes $h_{\ell,m}$ exhibit the simplest morphology when the binary system follows a quasicircular orbit with no spin-precession. The GW emitted by such a system displays a monotonically increasing behavior in both amplitude and frequency. In figure 1, the *top-left* plot shows the real part of $h_{2,2}$ for a quasicircular, aligned-spin (nonprecessing) system simulated using the Spectral Einstein Code (SpEC) [96–98] developed by the Simulating eXtreme Spacetime (SXS) collaboration [99]. We work with waveforms extrapolated to future null infinity, with extrapolation order $N = 2$. The latest catalog of SXS simulations includes memory by default [96, 100]. The memory correction is performed by adding the memory term to the extrapolated waveforms, which is computed using equation (11) in [96]. Unless stated otherwise, we undo this inclusion and work with memory removed waveforms (as will be expanded upon in section 2.5).

\ddagger While $t = 0$ according to this definition coincides with the merger time for most systems, this may not always hold for highly eccentric systems. To ensure that $t = 0$ corresponds to the merger time, one can define $t = 0$ as the time of the last peak in the waveform amplitude [61].

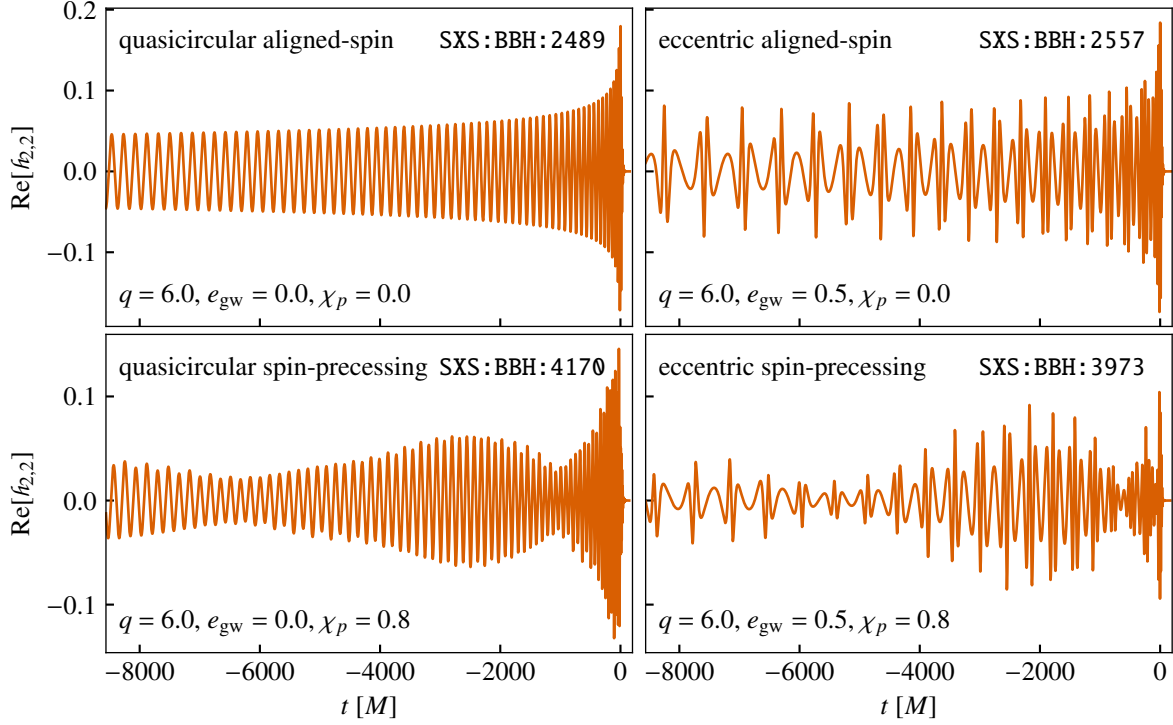


Figure 1. Effects of eccentricity and spin-precession on waveforms. *Top-left:* A quasicircular aligned-spin system, where we can see the monotonic increase of the amplitude and frequency. *Top-right:* An eccentric aligned-spin system, where modulations due to eccentricity are visible on the orbital timescale. *Bottom-left:* A quasicircular spin-precessing system, where modulations due to spin-precession are seen over the longer spin-precession timescale (spanning several orbits). *Bottom-right:* An eccentric spin-precessing system. Features of eccentricity on orbital-timescale and features of spin-precession on spin-precession timescale are simultaneously visible. In all panels, the eccentricity e_{gw} is measured at $t = -8000M$, following the procedure described in section 2.1. The inset texts indicate the simulation IDs from the SXS Catalog [96]. We have removed the memory contribution from these waveforms, which is included by default in the latest catalog of SXS waveforms.

By contrast, orbital eccentricity results in bursts of GW radiation at every pericenter (point of closest approach) passage [15, 16], which appear as modulations of the GW amplitude and frequency on the orbital-timescale. The *top-right* plot in figure 1 shows the real part of $h_{2,2}$ for an aligned-spin system on an eccentric orbit.

In an aligned-spin system, the spins of the black holes are either aligned or anti-aligned with respect to the orbital angular momentum \mathbf{L} which remains fixed throughout the system’s evolution. The $\hat{\mathbf{z}}$ direction of the binary’s source frame is chosen to be along \mathbf{L} by convention. In such systems, the direction of the strongest GWs emission is parallel and anti-parallel to \mathbf{L} . Consequently, the $(\ell = 2, m = \pm 2)$ modes remain the dominant modes during the binary’s entire evolution. In addition, due to the symmetry about the orbital plane (which lies on the $x - y$ plane), the negative and positive m modes are related by

$$h_{\ell,m} = (-1)^m h_{\ell,-m}^*, \quad (5)$$

where $*$ stands for complex conjugation. On the other hand, in a spin-precessing system, the black hole spins are tilted relative to the orbital angular momentum \mathbf{L} , causing the orbital angular momentum and the spins to precess around the total angular momentum of the system due to spin-spin and spin-orbit interactions [21]. Therefore, the \hat{z} direction of the source frame, which by convention is aligned with \mathbf{L} at a given reference time or frequency, no longer coincides with \mathbf{L} as the binary inspirals. This leads to leakage of GW power into $(\ell = 2, m \neq \pm 2)$ modes from the $(\ell = 2, m = \pm 2)$ modes causing modulation of the waveform on the longer spin-precession timescale, which occurs over several orbits. In figure 1, the *bottom-left* plot shows the real part of $h_{2,2}$ for a quasicircular spin-precessing system.

Finally, when the binary follows the most generic bound orbit, incorporating both spin-precession and eccentricity, the waveform modes exhibit the most complex morphology, showing the imprints of both effects. In figure 1, the *bottom-right* plot shows the real part of $h_{2,2}$ of an eccentric spin-precessing binary. The waveform shows modulations over orbital as well as spin-precession timescale.

2.3. Challenges in defining eccentricity in presence of spin-precession

Due to the leakage of GW power from the $(\ell = 2, m = \pm 2)$ modes to $(\ell = 2, m \neq \pm 2)$ modes in the inertial frame for a spin-precessing system, the $(2, 2)$ mode is not necessarily the dominant mode throughout the binary's evolution, and other $(\ell = 2, m \neq \pm 2)$ modes may become comparable at different times during the evolution (see e.g. figure 1 of [42]).

For an aligned-spin system on an eccentric orbit, the frequency ω_{22} of the inertial frame $(2, 2)$ mode exhibits the property that, while ω_{22} itself is nonmonotonic, ω_{22}^p (the values of ω_{22} at pericenters) and ω_{22}^a (the values of ω_{22} at apocenters) are monotonically increasing functions of time (see e.g. figure 1 of [90]). This property enables the construction of monotonic interpolants, $\omega_{22}^p(t)$ (the interpolant through ω_{22} at pericenters) and $\omega_{22}^a(t)$ (the interpolant through ω_{22} at apocenters). These monotonic interpolants were crucial for obtaining a consistent monotonic evolution of eccentricity in [90]. Thus, for aligned-spin systems, it suffices to work with the inertial frame $(2, 2)$ mode for extracting eccentricity information from its frequency evolution [90].

However, in spin-precessing systems, ω_{22}^p and ω_{22}^a computed in the inertial frame do not follow a monotonic trend. Therefore, the inertial-frame $(2, 2)$ mode frequency ω_{22} , on its own, is not suitable for measuring eccentricity in spin-precessing systems.

2.3.1. Coprecessing frame To address the challenges of defining eccentricity for a spin-precessing system, we aim to minimize the effects of spin-precession in the waveforms used for computing eccentricity. The primary challenge lies in leakage of GW power into $(\ell = 2, m \neq \pm 2)$ modes from $(\ell = 2, m = \pm 2)$ modes, which arises because the angular momentum \mathbf{L} evolves over time, while the frame used to decompose the waveform into spin-weighted spherical harmonics remains static. A straightforward solution to mitigate this is to transition to the coprecessing frame, which is a non-inertial, time-dependent frame where the \hat{z} -axis of the frame aligns with the direction of maximal gravitational wave emission

(which closely follows \mathbf{L}) at every instant [101–103]. The waveform modes $h_{\ell,m}$ are then expressed relative to this dynamic basis, thereby reducing the impact of precession of \mathbf{L} on the mode decomposition. This strategy has been used to simplify the modeling of spin-precessing waveforms in the quasicircular case [45–51] (and more recently in the eccentric case in [79]). In this work, we utilize the frame rotation functionality provided by the public library `scri` [104] to transform the waveform modes to the coprecessing frame. By design, the coprecessing frame ensures that the $(\ell = 2, m = \pm 2)$ modes remain the dominant modes throughout the binary’s evolution in this frame. For example, see the *middle* panel of figure 1 in [42].

Although, the mode hierarchy is reestablished in the coprecessing frame, it cannot get rid of all spin-precession effects. In particular, for spin-precessing systems, there exists no frame where the equation (5) is true [39], leading to a *mode asymmetry* between the positive and negative m modes for a given ℓ . In addition to the multiple-orbit-timescale motion of the orbital-plane described above, spin-precession induces waveform features varying on the orbital-timescale that cannot be removed by applying any rotation [39]. Therefore, even in the coprecessing frame, the frequency of the $(2, 2)$ mode is not guaranteed to have a monotonically increasing frequency at the pericenters and apocenters. One can, however, get around this by noticing that, at any given instant, the (ℓ, m) and $(\ell, -m)$ modes are affected nearly oppositely by the spin-precession [39–42]. Consequently, the $(2, 2)$ and $(2, -2)$ modes alternately dominate the GW power on the orbital-timescale, as illustrated in figure 2 through their frequencies. We denote the quantities in the coprecessing frame using the superscript “copr”.

To generalize the definition of eccentricity to spin-precessing systems, one could try to replace ω_{22}^p and ω_{22}^a in section 2.3 with the values of $\omega_{2,2}^{\text{copr}}$ and $\omega_{2,-2}^{\text{copr}}$ evaluated at the pericenters and apocenters. However, spin-induced orbital-timescale effects break the monotonicity of the values of $\omega_{2,2}^{\text{copr}}(t)$ and $\omega_{2,-2}^{\text{copr}}(t)$ at their extrema (interpolants through these quantities at the pericenters are denoted as $\omega_{2,2}^{\text{copr,p}}$ and $\omega_{2,-2}^{\text{copr,p}}$ in figure 2). To mitigate this, we follow [39–42], and define quantities in the coprecessing frame by combining the $(2, 2)$ and $(2, -2)$ modes

$$A_{\text{gw}} = \frac{1}{2} (A_{2,2}^{\text{copr}} + A_{2,-2}^{\text{copr}}), \quad (6)$$

$$\phi_{\text{gw}} = \frac{1}{2} (\phi_{2,2}^{\text{copr}} - \phi_{2,-2}^{\text{copr}}), \quad (7)$$

$$\omega_{\text{gw}} = \frac{d\phi_{\text{gw}}}{dt} = \frac{1}{2} (\omega_{2,2}^{\text{copr}} - \omega_{2,-2}^{\text{copr}}). \quad (8)$$

In literature, these quantities have previously been denoted as A_+ , ϕ_- and ω_- , respectively (see e.g. equations (48) and (49) in [41]). We use the notation in equations (6)-(8) for convenience in the equations that appear in the rest of the paper.

In case of an aligned-spin system, quantities in equations (6)-(8) reduce to the corresponding values of the $(2, 2)$ mode because the inertial and coprecessing frames are equivalent in aligned-spin systems, and the negative and positive m modes are related via equation (5) due to the symmetry about the orbital plane.

The *bottom* panel of figure 2 shows the coprecessing frame frequencies $\omega_{2,2}^{\text{copr}}$ and $\omega_{2,-2}^{\text{copr}}$ and their antisymmetric combination ω_{gw} . These frequencies correspond to an NR waveform

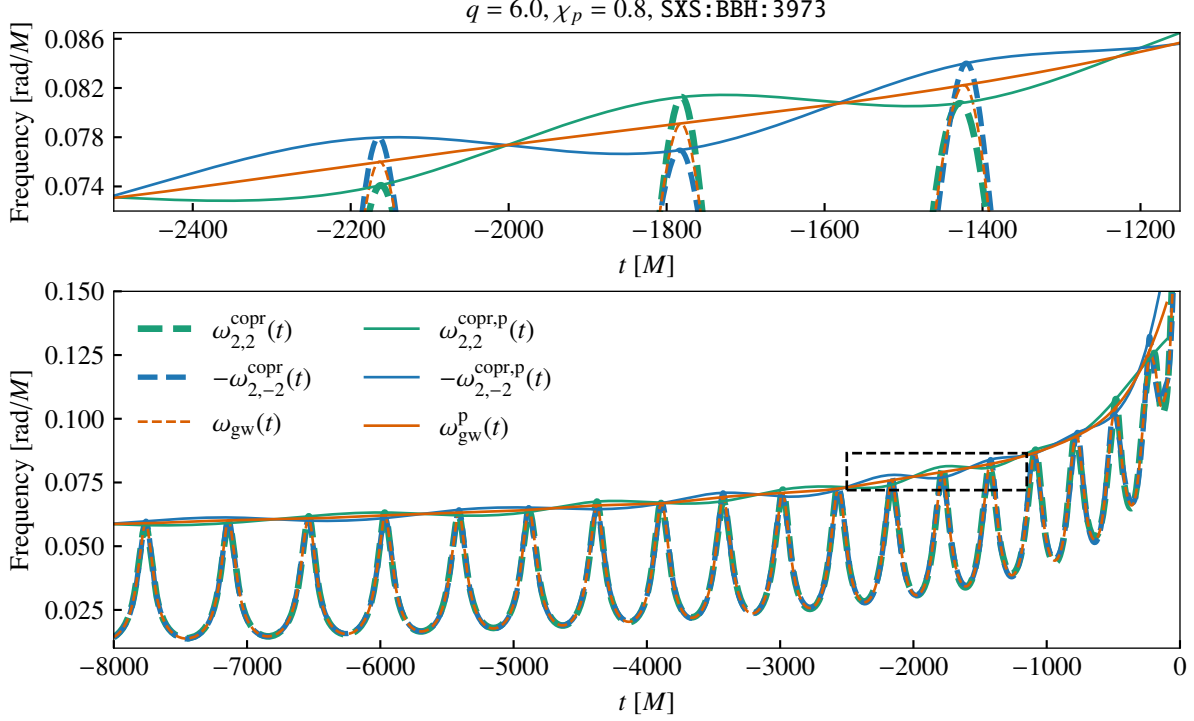


Figure 2. GW frequency in the coprecessing frame. *Bottom:* Shows the coprecessing frame frequencies $\omega_{2,2}^{\text{copr}}$, $\omega_{2,-2}^{\text{copr}}$, and their antisymmetric combination ω_{gw} as dashed curves of different thickness. It also shows the interpolants through their values at their respective local maxima (denoted by a superscript “p” for *pericenters*) as solid curves. Both $\omega_{2,2}^{\text{copr}}$ and $\omega_{2,-2}^{\text{copr}}$ exhibit a reduced influence of spin-precession compared to their inertial frame counterparts, and closely resemble the frequency evolution of an aligned-spin system. However, they still retain orbital-timescale spin-induced effects, as highlighted in the *top* panel. *Top:* A zoomed-in view of the boxed region in the bottom panel. Spin-precession affects $\omega_{2,2}^{\text{copr}}$ and $\omega_{2,-2}^{\text{copr}}$ in nearly opposite ways on the orbital-timescale, leading to their alternate dominance. As a result, the values of these frequencies at the pericenters becomes oscillatory, introducing nonmonotonicity in their interpolants (solid blue and green). In contrast, ω_{gw} displays a monotonic increase in its values at the pericenters (solid orange). The system has an eccentricity $e_{\text{gw}} = 0.5$ at $t = -8000M$.

of an eccentric spin-precessing system SXS:BBH:3973 with $q = 6$ and $\chi_p = 0.8$. The panel also shows the interpolants (denoted by a superscript “p”) of their values at the pericenters. The *top* panel focuses on a region near the pericenters (boxed region in the *bottom* panel). While $\omega_{2,2}^{\text{copr,p}}$ and $\omega_{2,-2}^{\text{copr,p}}$ at the extrema dominate alternately, the values at extrema for $\omega_{\text{gw}}^{\text{p}}$ increase monotonically.

As an alternative to ω_{gw} , one can also define a rotationally covariant angular velocity, defined as the velocity of the rotating frame that minimizes the time dependence of the modes [105]. However, since we find no significant difference between this angular velocity and ω_{gw} , we choose to use ω_{gw} to define e_{gw} .

2.4. Generalized eccentricity definition

We extend the definition of eccentricity to spin-precessing systems using the GW frequency ω_{gw} defined in equation (8). The steps for computing e_{gw} and l_{gw} are identical to those outlined in section II.H of [90], with one key distinction: we use the variables A_{gw} , ϕ_{gw} , and ω_{gw} (defined in Eqs. (6), equation (7), and equation (8), respectively) instead of the corresponding quantities from the (2, 2) mode in the inertial frame. First we define $e_{\omega_{\text{gw}}}$ using ω_{gw} ,

$$e_{\omega_{\text{gw}}}(t) = \frac{\sqrt{\omega_{\text{gw}}^{\text{p}}(t)} - \sqrt{\omega_{\text{gw}}^{\text{a}}(t)}}{\sqrt{\omega_{\text{gw}}^{\text{p}}(t)} + \sqrt{\omega_{\text{gw}}^{\text{a}}(t)}}. \quad (9)$$

Here, $\omega_{\text{gw}}^{\text{p}}(t)$ and $\omega_{\text{gw}}^{\text{a}}(t)$ are the interpolants through the ω_{gw} values at the pericenters ($\omega_{\text{gw}}^{\text{p}}$) and apocenters ($\omega_{\text{gw}}^{\text{a}}$), respectively. We then define the eccentricity e_{gw} using the following transformation to ensure that it correctly exhibits the Newtonian limit [89].

$$e_{\text{gw}}(t) = \cos\left(\frac{\Psi(t)}{3}\right) - \sqrt{3} \sin\left(\frac{\Psi(t)}{3}\right), \quad (10)$$

where

$$\Psi(t) = \arctan\left(\frac{1 - e_{\omega_{\text{gw}}}^2(t)}{2e_{\omega_{\text{gw}}}(t)}\right). \quad (11)$$

Once we obtain the pericenter times t^{p} , the mean anomaly between two successive pericenters, t_i^{p} and t_{i+1}^{p} , can be defined over the interval $t_i^{\text{p}} \leq t < t_{i+1}^{\text{p}}$ as

$$l_{\text{gw}}(t) = 2\pi \frac{t - t_i^{\text{p}}}{t_{i+1}^{\text{p}} - t_i^{\text{p}}}. \quad (12)$$

To construct the interpolants $\omega_{\text{gw}}^{\text{p}}(t)$ and $\omega_{\text{gw}}^{\text{a}}(t)$, we require the values of ω_{gw} at the pericenters and apocenters, respectively. These are identified as the local maxima and minima of either ω_{gw} or A_{gw} . However, in systems with small eccentricity, these extrema can be difficult to detect directly due to the eccentric modulations becoming small compared to the secular growth in ω_{gw} or A_{gw} . To address this, we work with the residuals obtained by subtracting the secular trend from ω_{gw} or A_{gw} , thereby enhancing the prominence of the oscillatory features. The secular trend can be estimated either by fitting a power-law model inspired by PN expressions in the quasicircular limit (this choice using A_{gw} is referred to as **AmplitudeFits** [90]), or by using the amplitude or frequency of a corresponding quasicircular waveform (this choice using A_{gw} is referred to as **ResidualAmplitude** [90]). The quasicircular waveform is generated using the same binary parameters as the eccentric waveform, with the eccentricity set to zero. A detailed discussion of various methods for locating extrema using frequency- and amplitude-derived quantities can be found in Section III of [90]. Since the locations of the extrema may vary slightly depending on the choice of data, the extrema-finding procedure should be regarded as a part of the eccentricity definition. In this work, unless stated otherwise, we use the **AmplitudeFits** method to locate the extrema for measuring eccentricity and mean anomaly throughout the rest of the paper.

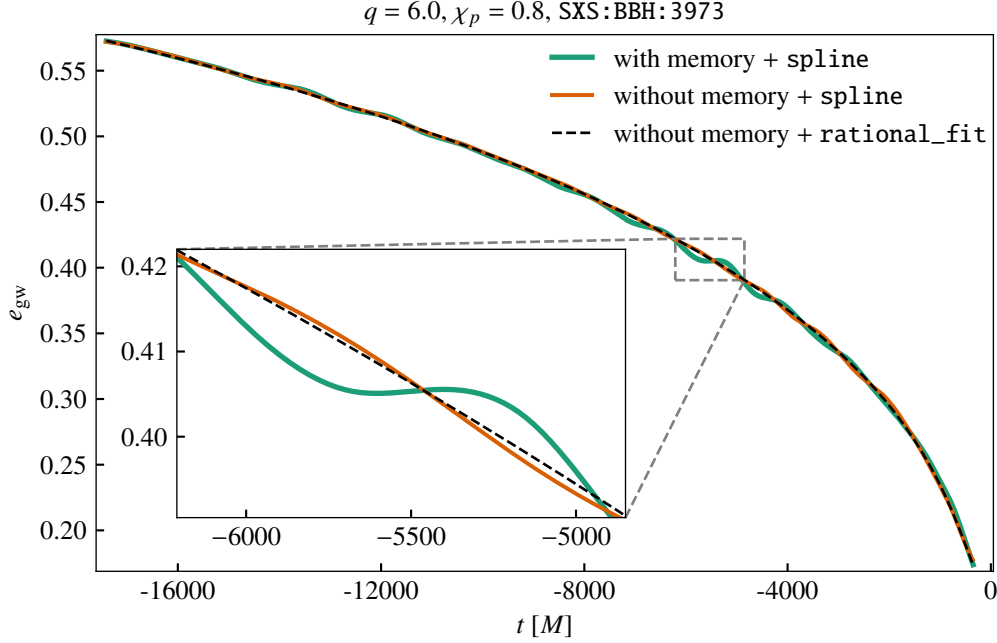


Figure 3. Effect of memory on $e_{\text{gw}}(t)$. For unequal mass and highly spin-precessing systems, the memory causes visible oscillations in the measured $e_{\text{gw}}(t)$. The $e_{\text{gw}}(t)$ after memory removal gets rid of most of these oscillations. Some oscillations remain in $e_{\text{gw}}(t)$ even after memory removal, which go away when we switch from `spline` interpolation to `rational_fit` when constructing the $\omega_{22}^{\text{p}}(t)$ and $\omega_{22}^{\text{a}}(t)$ interpolants in equation (9) (discussed in detail in section 2.6). The $e_{\text{gw}}(t)$ before and after removal of memory is shown for SXS:BBH:3973.

Finally, ϕ_{gw} is used for internal diagnostics and for estimating the orbital period when necessary. One must also be cautious about numerical noise and ensure that the identified extrema arise from genuine eccentricity-induced modulations, rather than spurious fluctuations. Since eccentricity leads to oscillations on the orbital-timescale, the phase difference in ϕ_{gw} between two consecutive extrema should be approximately 4π (as ω_{gw} is roughly twice the orbital frequency). We use this criterion to discard extrema that are likely due to numerical noise.

2.5. Effects of waveform memory

Our goal is to extract the orbital eccentricity from the GW signal. However, unlike the orbital dynamics, the waveforms at future null infinity can contain imprints of additional effects, such as gravitational memory [106–112]. Therefore, e_{gw} computed using GW can inherit a memory dependence. This can be attributed to the fact that memory effect alters the average amplitude of the waveform modes, which in turn, affects the transformation of the waveform to the coprecessing frame and the quantities such as $\omega_{\text{gw}}^{\text{p}}(t)$ and $\omega_{\text{gw}}^{\text{a}}(t)$ used to define e_{gw} . More specifically, the angular momentum operator, when applied on the waveform modes, returns an extra term due to the memory contribution (see the discussion around equation (11) and (12) in [105]), which can impact the direction of maximal GW emission used to define the

coprecessing frame.

To avoid this, we perform memory removal from the waveforms before using them to measure e_{gw} . In figure 3, we demonstrate the effect of memory on e_{gw} for an unequal mass ($q = 6$) and highly spin-precessing ($\chi_p = 0.8$) NR waveform. Without memory removal the e_{gw} curve has small oscillations which are reduced when we use waveforms after memory removal. Some modulations remain in $e_{\text{gw}}(t)$ even after memory removal, which go away with `rational_fit` interpolation for $\omega_{\text{gw}}^{\text{p}}(t)$ and $\omega_{\text{gw}}^{\text{a}}(t)$, which will be discussed in the next section. Throughout the rest of the paper, we will use waveforms after memory removal.

2.6. Rational Fits for $\omega_{\text{gw}}^{\text{p}}(t)$ and $\omega_{\text{gw}}^{\text{a}}(t)$

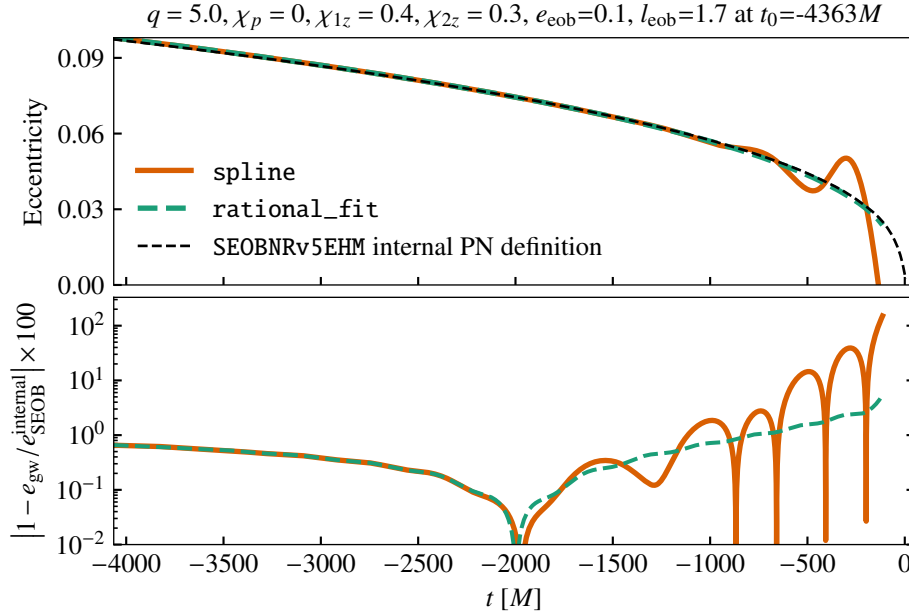


Figure 4. Comparison of Interpolation Methods. *Top:* $e_{\text{gw}}(t)$ measured (using `ResidualAmplitude`) from a waveform generated using `SEOBNRv5EHM`, with the initial input parameters specified in the plot title, where e_{eob} and l_{eob} are the initial input model eccentricity and mean anomaly, respectively, at the starting time t_0 . Using `spline` for $\omega_{\text{gw}}^{\text{p}}(t)$ and $\omega_{\text{gw}}^{\text{a}}(t)$ leads to nonmonotonic oscillations in the computed e_{gw} near the merger. In contrast, when using the rational function approximation (`rational_fit`), the resulting e_{gw} is free of these oscillations. For reference, we also include the eccentricity $e_{\text{SEOB}}^{\text{internal}}$, the internal definition of eccentricity in the Keplerian parametrization of the conservative dynamics in `SEOBNRv5EHM`. *Bottom:* the instantaneous percentage difference between e_{gw} using `spline` or `rational_fit` and $e_{\text{SEOB}}^{\text{internal}}$.

The definition of eccentricity e_{gw} in equation (10) relies on the interpolants $\omega_{22}^{\text{p}}(t)$ and $\omega_{22}^{\text{a}}(t)$. In our previous work in [90], we used Cubic interpolating splines§ to build these interpolants. We find that while such interpolants work very well for most part of the inspiral, they can struggle at times close to the merger. Near the merger, the spline interpolants

§ Uses `scipy.interpolate.InterpolatedUnivariateSpline`

introduces artificial oscillations in the measured e_{gw} (see figure 4). To avoid such oscillations in e_{gw} near the merger, we seek alternative interpolation methods that are robust near the merger.

Following previous works [91], we employ an alternative interpolation method for modeling $\omega_{\text{gw}}^{\text{p}}(t)$ and $\omega_{\text{gw}}^{\text{a}}(t)$ using rational functions. While [91] uses rational function of the form $(a + bx)/(1 + cx)$, we find it to be less effective for fitting $\omega_{\text{gw}}^{\text{p}}(t)$ and $\omega_{\text{gw}}^{\text{a}}(t)$ for longer waveforms. Therefore, we build the interpolants using rational functions with higher numerator and denominator degrees when required. Specifically, we employ the “Stabilized Sanathanan-Koerner” iterations to build rational approximations [113]. We refer to this method simply as `rational_fit`.

To ensure that the $\omega_{\text{gw}}^{\text{p}}(t)$ and $\omega_{\text{gw}}^{\text{a}}(t)$ interpolants are both monotonically increasing and accurate, we carefully select an optimal pair of numerator and denominator degrees for the rational function approximation algorithm. If the degrees are too high, spurious divergences may appear in the interpolants; if too low, the resulting interpolants may be insufficiently accurate. To address this, we adaptively adjust the numerator and denominator degrees used in the rational function approximation algorithm.

We begin with an initial guess for the degrees based on the approximate number of orbital cycles (which can be estimated from the number of local extrema) in the waveform. We then compute the first time derivative of the resulting interpolant. If this derivative is strictly monotonic, we increment both degrees by one to improve accuracy and repeat the process. If the derivative is not strictly monotonic, the chosen degrees are too high, and we reduce them by one until monotonicity is restored or the degrees reach a minimum value of one. This iterative procedure eliminates divergences in the interpolants and ensures a smooth, monotonically increasing evolution of e_{gw} when using `rational_fit`.

We find that `rational_fit` performs as robustly and accurately as `spline` in regions far from the merger while showing superior robustness and accuracy near the merger. This is evident in figure 4, where the *top* panel compares e_{gw} obtained using `spline` and `rational_fit` to $e_{\text{SEOB}}^{\text{internal}}$, the internal definition of eccentricity in the Keplerian parametrization of the conservative dynamics in SEOBNRv5EHM [60, 61]. The *bottom* panels shows the instantaneous percentage difference. Figure 4 demonstrates that `rational_fit` provides a measurement of e_{gw} that is more consistent with $e_{\text{SEOB}}^{\text{internal}}$, while being free of the spurious oscillations present in `spline` near the merger. In Appendix A, we compare these two methods on a larger set of waveforms to assess their robustness. We find that the differences between $e_{\text{SEOB}}^{\text{internal}}$ and e_{gw} can reach $\sim 1000\%$ when using `spline`, especially for small eccentricities ($e_{\text{gw}} \lesssim 5 \times 10^{-2}$) and near the merger. For the same cases, the differences between $e_{\text{SEOB}}^{\text{internal}}$ and e_{gw} fall within 10% with `rational_fit`.

In addition to providing robust interpolation near the merger, `rational_fit` is also less susceptible to small oscillations in the inspiral that may arise due to numerical noise, and provides smoother monotonically decreasing e_{gw} compared to `spline`. When building the $\omega_{\text{gw}}^{\text{p}}(t)$ and $\omega_{\text{gw}}^{\text{a}}(t)$ interpolants, `rational_fit` minimizes the root mean square error between the data and the approximation rather than strictly interpolate through the data points. Thus it

|| We use the Python implementation `polyrat.StabilizedSKRationalApproximation` of the algorithm [113, 114]

approximates the overall trend of the data which helps avoid local fluctuations present when using `spline`. Nevertheless, one must be cautious when using the GW frequency obtained from noisy NR waveforms, as it can lead to spurious oscillations in e_{gw} . In [Appendix B](#) we discuss how the oscillations in e_{gw} computed with `gw_eccentricity` [90] noted by [93] arise mainly due to numerical noise in the NR waveforms, and how `rational_fit` is less susceptible to such oscillations.

Similar to numerical noise, memory effects can also introduce oscillations in $e_{\text{gw}}(t)$ as discussed in [section 2.5](#). While removing the memory significantly suppresses these oscillations, some residual oscillations remain in $e_{\text{gw}}(t)$ when computed using `spline`. These residual oscillations disappear when using `rational_fit`, as shown in [figure 3](#). Throughout the rest of the paper, we will use `rational_fit` when computing e_{gw} .

2.7. Small eccentricity & large spin-precession regime

By transforming the waveform to the coprecessing frame, we are able to remove the effects of the precession of the orbital plane on the waveform to a large extent. However, as discussed in [section 2.3.1](#), the waveform in the coprecessing frame still exhibits mode asymmetry caused by spin-precession. The effect of mode asymmetry on e_{gw} is reduced by using ω_{gw} instead of $\omega_{2,2}^{\text{copr}}$ in defining eccentricity in [equation \(10\)](#). While this is sufficient to obtain a monotonically decreasing $e_{\text{gw}}(t)$ for large eccentricity, we need to take further steps to ensure correct $e_{\text{gw}}(t)$ measurement in the small eccentricity and large spin-precession regime.

One can express ω_{gw} as the sum of a secular, monotonically increasing trend ($\omega_{\text{gw}}^{\text{secular}}$) caused by radiation reaction and modulations arising due to eccentricity ($\delta\omega_{\text{gw}}^{\text{ecc}}$) and spin-induced effects ($\delta\omega_{\text{gw}}^{\text{spin}}$) [[115–117](#)]:

$$\omega_{\text{gw}} = \omega_{\text{gw}}^{\text{secular}} + \delta\omega_{\text{gw}}^{\text{ecc}} + \delta\omega_{\text{gw}}^{\text{spin}}. \quad (13)$$

The amplitude of $\delta\omega_{\text{gw}}^{\text{spin}}$, compared to $\delta\omega_{\text{gw}}^{\text{ecc}}$, depends on the eccentricity e_{gw} , the spin-precession parameter χ_p , and the mass ratio q of the system. For large eccentricity, $\delta\omega_{\text{gw}}^{\text{spin}} \ll \delta\omega_{\text{gw}}^{\text{ecc}}$. However, at smaller eccentricities, the spin-induced oscillation $\delta\omega_{\text{gw}}^{\text{spin}}$ can become non-negligible compared to $\delta\omega_{\text{gw}}^{\text{ecc}}$, particularly in highly spin-precessing ($\chi_p \sim 1$) and asymmetric ($q \gg 1$) systems, where it may even dominate over $\delta\omega_{\text{gw}}^{\text{ecc}}$. Similar features can be observed in the dynamical variables of eccentric spin-precessing systems. For example, the `SpEC` [[97](#)] code employs an eccentricity control algorithm based on fitting $\dot{\Omega}_{\text{orb}}$, the first derivative of the orbital angular frequency Ω_{orb} computed from the black hole trajectories, where $\dot{\Omega}_{\text{orb}}$ is written as a sum of three terms analogous to [equation \(13\)](#) (see e.g. [equation \(47\)](#) of [[115](#)], [equation \(4\)](#) of [[117](#)], and [equation \(5\)](#) of [[116](#)]).

In this section, we focus on an example NR simulation `SXS:BBH:4438` with $q = 3$ and $\chi_p = 0.8$. The system has an initial eccentricity $e_{\text{gw}} \approx 5 \times 10^{-3}$ at $t_0 \approx -6000M$. Due to the small eccentricity and large spin-precession, spin-induced features in ω_{gw} are non-negligible. We discuss procedures for accurately estimating e_{gw} in such a system by removing spin-induced features from the waveform quantities.

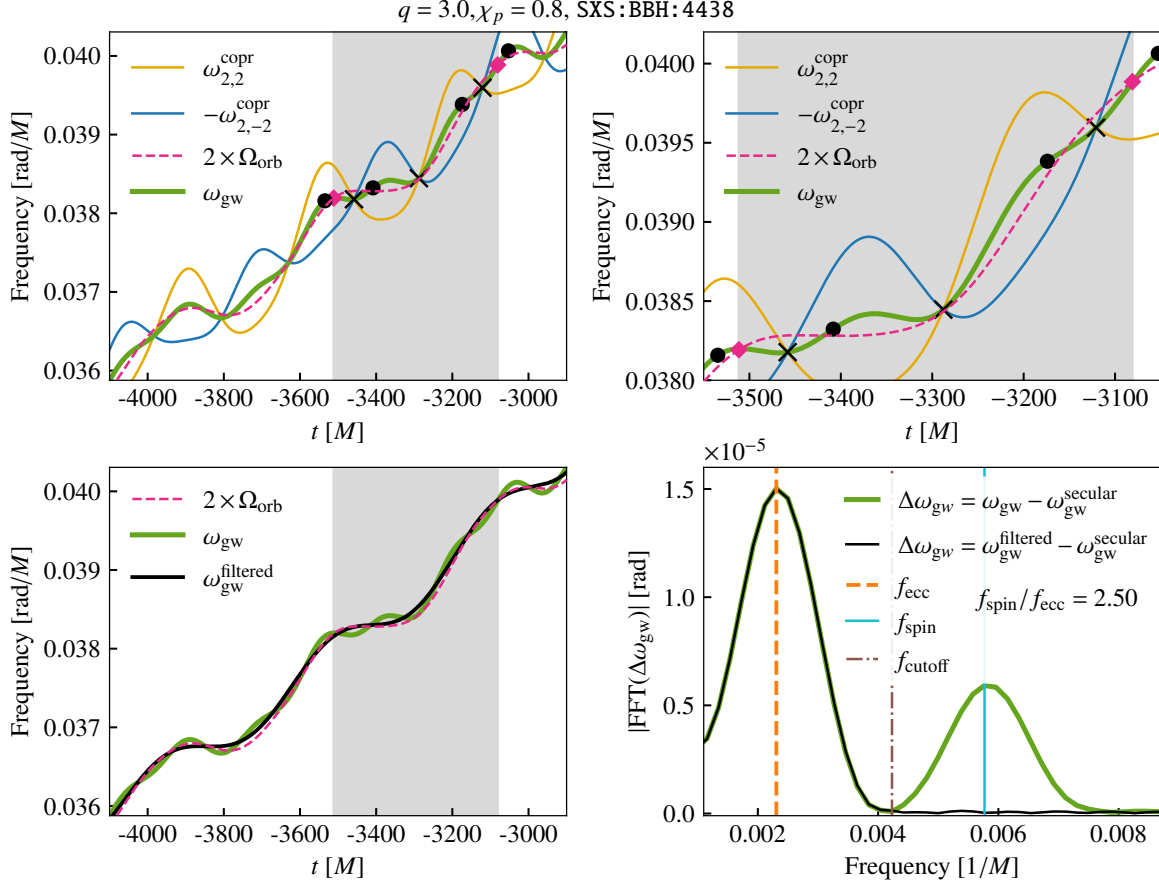


Figure 5. Spin-induced modulations in ω_{gw} for a low-eccentricity, high-spin-precession system SXS:BBH:4438. *Top-left:* ω_{gw} , defined as the antisymmetric combination of $\omega_{2,2}^{\text{copr}}$ and $\omega_{2,-2}^{\text{copr}}$, exhibits orbital-scale oscillations due to eccentricity and faster spin-induced modulations. The eccentricity-induced oscillations resemble those in the orbital angular frequency Ω_{orb} . The shaded region spans one orbit, bounded by two consecutive pericenters (pink diamonds) in Ω_{orb} . *Top-right:* Zoom-in of the shaded region. The shaded region (one eccentric oscillation) contains ~ 2.5 spin-induced oscillations; each oscillation is marked by two consecutive local peaks (dark circles) in ω_{gw} . As explained in section 2.7.1, these spin-induced oscillations be associated with the intersections of $\omega_{2,2}^{\text{copr}}$ and $\omega_{2,-2}^{\text{copr}}$ (crosses). *Bottom-right:* Amplitude spectra of $(\omega_{\text{gw}} - \omega_{\text{gw}}^{\text{secular}})$ and $(\omega_{\text{gw}}^{\text{filtered}} - \omega_{\text{gw}}^{\text{secular}})$ reveal the frequency components. The high-frequency mode associated with spin-induced oscillations is suppressed after filtering. *Bottom-left:* Spin-induced modulations are removed using a low-pass filter with a cutoff frequency (f_{cutoff}) located at the trough between the eccentric mode (f_{ecc}) and the spin-induced mode (f_{spin}) in the amplitude spectrum shown in the *Bottom-right* panel.

2.7.1. Identifying the timescales To remove the spin-induced oscillations from ω_{gw} , we need to identify the timescale of these oscillations. We can achieve this by either looking at the local extrema in these modulations in time domain or looking at the amplitude spectra of the waveform modes in the frequency domain.

The *top-left* panel of figure 5 shows ω_{gw} of SXS:BBH:4438. For comparison, it also shows $\omega_{2,2}^{\text{copr}}$, $\omega_{2,-2}^{\text{copr}}$ and $2 \times \Omega_{\text{orb}}$. We use the time between two consecutive peaks in these frequencies to estimate the characteristic timescale of the modulations in them. These “peaks” and “troughs” are obtained after subtracting the secular trend from the respective frequency (using a method similar to the `FrequencyFits` method from [90]): for this reason, the peaks and troughs that are identified in figure 5 may not correspond exactly with the points one might associate by eye as turnover points.

The area around the shaded region in the *top-left* panel of figure 5 is zoomed-in in the *top-right* panel. The shaded region spans one orbit bounded by the two local peaks (pink diamonds) of Ω_{orb} . The amplitude of the oscillation in $\omega_{2,2}^{\text{copr}}$ and $\omega_{2,-2}^{\text{copr}}$ are much larger compared to the same in $2 \times \Omega_{\text{orb}}$. ω_{gw} shows oscillations of smaller amplitude compared to those in $\omega_{2,2}^{\text{copr}}$, and closely follows the orbital-timescale oscillations due to eccentricity in $2 \times \Omega_{\text{orb}}$. However, some spin-induced modulations are visible in ω_{gw} : a local trough forms in ω_{gw} near the intersections (crosses) of $\omega_{2,2}^{\text{copr}}$ and $\omega_{2,-2}^{\text{copr}}$, leading to corresponding local peaks (dark circles) in ω_{gw} between these intersection points. We associate these shorter timescale oscillations with spin-induced effects ($\delta\omega_{\text{gw}}^{\text{spin}}$ in equation (13)), as they arise from asymmetries between $\omega_{2,2}^{\text{copr}}$ and $\omega_{2,-2}^{\text{copr}}$.

Henceforth, we refer to frequency of the spin-induced oscillations in ω_{gw} (i.e. due to $\delta\omega_{\text{gw}}^{\text{spin}}$) as f_{spin} , and the frequency of the eccentricity-induced oscillations (i.e. due to $\delta\omega_{\text{gw}}^{\text{ecc}}$) as f_{ecc} . In figure 5, one eccentric oscillation (shaded region between the two pink diamonds) contains ~ 2.5 spin-induced oscillations, where one spin-induced oscillation spans two consecutive local peaks indicated by dark circles. Therefore, the frequency f_{spin} is approximately $2.5 \times f_{\text{ecc}}$. We can verify the relation between f_{ecc} and f_{spin} by looking at the amplitude spectrum of the residual frequency $\Delta\omega_{\text{gw}} = \omega_{\text{gw}} - \omega_{\text{gw}}^{\text{secular}}$ (obtained using a method similar to `FrequencyFits`) in the *bottom-right* panel of figure 5. The amplitude spectrum has two modes at the two frequencies f_{ecc} and f_{spin} related to the eccentric and the spin-induced oscillations, respectively, with $f_{\text{spin}}/f_{\text{ecc}} = 2.5$ consistent with the inference from the timescales in the *top-right* panel. In general, across the inspiral, we find that $f_{\text{spin}}/f_{\text{ecc}} \sim 2 - 3$ which is consistent with [117] (see their figure 3) although in [117] the oscillations are in $\dot{\Omega}_{\text{orb}}$. To summarize, f_{spin} and f_{ecc} can be extracted in two ways: either from the local peaks of $\Delta\omega(t)$ in the time domain, or from the peaks in its amplitude spectrum. In the remainder of this work, we refer to the values of f_{spin} and f_{ecc} obtained from the amplitude spectrum.

2.7.2. Removing spin induced effects using low-pass filter In the previous section, we noticed that $f_{\text{spin}} \approx n f_{\text{ecc}}$, where n varies between 2 to 3 across the inspiral. Therefore, one can remove the spin-induced oscillations by applying a low-pass filter on $\Delta\omega_{\text{gw}}$ with the cutoff frequency f_{cutoff} chosen appropriately such that $f_{\text{ecc}} < f_{\text{cutoff}} < f_{\text{spin}}$. Such a method has been applied to remove the spin-induced oscillation from $\dot{\Omega}_{\text{orb}}$ in [117]. We follow a similar procedure as outlined in section II.B.1 of [117].

Because the orbital period decreases over time as the binary inspirals, using a fixed f_{cutoff} to perform low-pass filter for the entire ω_{gw} may not always be effective, especially for longer waveforms. Therefore, we need to perform the low-pass filter on ω_{gw} segment-wise, where each segment may span a few orbits such that both eccentric and spin-induced oscillations are captured within the segment, and at the same time, f_{spin} and f_{ecc} remains nearly constant across the segment. If $\Delta T(t)$ is the timescale of the spin-induced modulations at t , then a segment of size $10 \times \Delta T(t)$, centered around t , would contain $\sim 3 - 5$ orbital cycles since one orbital cycle contains $\sim 2 - 3$ spin-induced oscillations (as discussed above). As discussed in the previous section, ΔT can be estimated by finding the time difference between consecutive local peaks in $\Delta\omega_{\text{gw}}$. However, we employ an easier alternative approach to find ΔT by looking at the time difference between the consecutive intersection points of $\omega_{2,2}^{\text{copr}}$ and $\omega_{2,-2}^{\text{copr}}$ since the intersection points can be associated with the local troughs in ω_{gw} (see figure 5).

Assuming there are $N + 1$ such intersection points, we compute the gaps $\{\Delta T_i = T_{i+1} - T_i\}_{i=1,\dots,N}$ between the intersection points $\{T_i\}_{i=1,\dots,N+1}$, and associate each ΔT_i with the time at the midpoint $\{t_i = (T_{i+1} + T_i)/2\}_{i=1,\dots,N}$. We use these data points $\{(t_i, \Delta T_i)\}_{i=1,\dots,N}$, to construct an interpolant $\Delta T^{\text{intersect}}(t)$ for the period of the occurrences of the intersection points. An interpolant for the frequency of spin-induced oscillations is then obtained as $f_{\text{spin}}^{\text{intersect}}(t) = 1/\Delta T^{\text{intersect}}(t)$. Note that we do not use $f_{\text{spin}}^{\text{intersect}}(t)$ directly for low-pass filtering. Instead, it serves as an initial estimate to guide the accurate extraction of f_{spin} from the amplitude spectrum of $\Delta\omega_{\text{gw}}(t)$ (step (b) below).

We use the following steps to filter out the spin-induced oscillations in ω_{gw} and obtain the filtered frequency $\omega_{\text{gw}}^{\text{filtered}}$ containing only eccentricity induced oscillations:

- (a) To ensure that we are using a suitable f_{cutoff} , we process the data using overlapping segments. The overlapping segments are of a varying size set as $10 \times \Delta T^{\text{intersect}}(t_s)$, where t_s is the time at the center of the segment. The times $\{t_s\}$ are selected at regular intervals of size $5 \times \min(\Delta T^{\text{intersect}}(t))$ to ensure some overlap between successive segments.
- (b) For each segment, we compute the residual $\Delta\omega_{\text{gw}}(t)$. We compute the Fast Fourier transform of $\Delta\omega_{\text{gw}}(t)$ and denote it as $\text{FFT}(\Delta\omega_{\text{gw}})(f)$. We search for the modes related to the eccentric and spin-induced oscillations in the amplitude spectrum $|\text{FFT}(\Delta\omega_{\text{gw}})| (f)$ by locating the local frequency peaks using `scipy.signal.find_peaks` from Scipy [118]. To locate f_{ecc} , we restrict the search to the range $(1/4)f_{\text{spin}}^{\text{intersect}}(t_{\text{mid}}) \leq f_{\text{ecc}} \leq (1/2)f_{\text{spin}}^{\text{intersect}}(t_{\text{mid}})$, where t_{mid} is the midpoint of the current segment and we use the $f_{\text{spin}}^{\text{intersect}}(t)$ interpolant obtained earlier. Similarly, we restrict the search for f_{spin} to the range $f_{\text{spin}} \geq (3/4)f_{\text{spin}}^{\text{intersect}}(t_{\text{mid}})$. See *bottom-right* panel of figure 5 for an example, where we can see two distinct peaks: the peak at higher frequency corresponds to f_{spin} and the peak at the lower frequency corresponds to f_{ecc} .
- (c) We then set the cut-off frequency f_{cutoff} to the frequency at the local trough between f_{ecc} and f_{spin} . We apply a low-pass filter and set $|\text{FFT}(\Delta\omega_{\text{gw}})|$ to zero for frequencies greater than f_{cutoff} and take inverse Fourier transform to obtain the filtered residual $\Delta\omega_{\text{gw}}^{\text{filtered}}$. Finally, we get the filtered ω_{gw} as $\omega_{\text{gw}}^{\text{filtered}} = \Delta\omega_{\text{gw}}^{\text{filtered}} + \omega_{\text{gw}}^{\text{secular}}$, where $\omega_{\text{gw}}^{\text{secular}}$ is secular trend in ω_{gw} . The *bottom-left* panel of figure 5 shows the filtered frequency $\omega_{\text{gw}}^{\text{filtered}}$ which

closely resembles $2 \times \Omega_{\text{orb}}$. The *bottom-right* panel shows the amplitude spectrum of the residual of the filtered frequency, that is, $(\omega_{\text{gw}}^{\text{filtered}} - \omega_{\text{gw}}^{\text{secular}})$ which no longer contains the modes at f_{spin} present in the unfiltered case.

- (d) The filtered overlapping segments are combined using a blending function to obtain the full filtered time series. We use `numpy.hanning` from the Numpy library for smooth blending.

So far, we have described the spin-induced oscillations in ω_{gw} . Similar features also appear in the amplitude A_{gw} . Since amplitude based methods, like the `AmplitudeFits`, locate the pericenters and apocenters using the local extrema in A_{gw} or quantities derived from A_{gw} , it is necessary to remove the spin-induced oscillations from A_{gw} as well. The procedure to remove the spin-induced oscillations from A_{gw} is the same as described above for ω_{gw} .

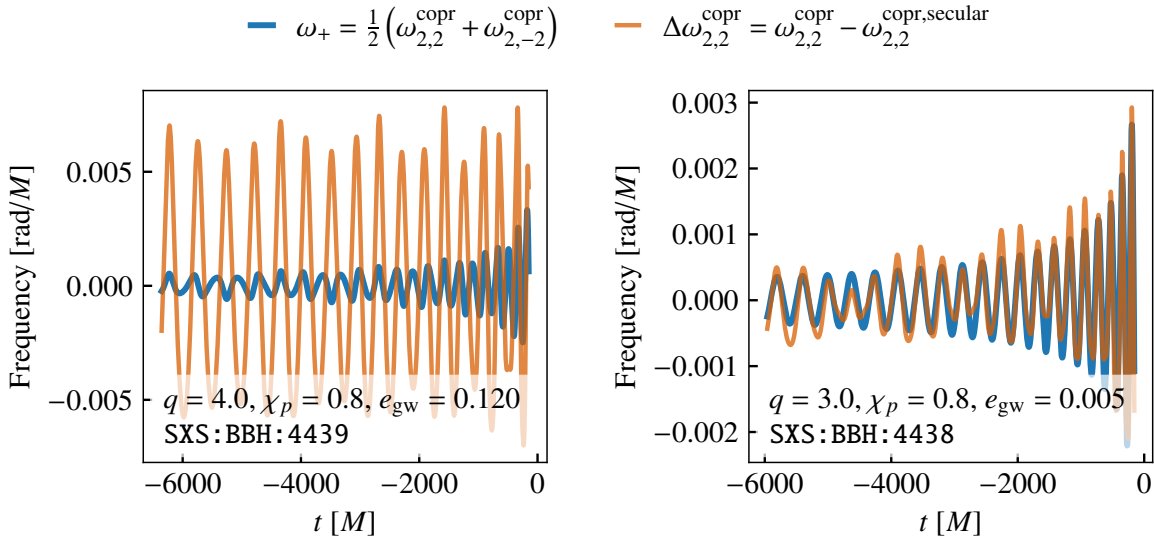


Figure 6. Requirement for filtering. *Left:* ω_+ is smaller compared to the residual coprecessing frequency $\Delta\omega_{2,2}^{\text{copr}}$, and, therefore, filtering ω_{gw} is not required. *Right:* Amplitude of the ω_+ is nearly the same as the amplitude of $\Delta\omega_{2,2}^{\text{copr}}$. In this case, filtering is required to remove the non-negligible spin-induced effect.

2.7.3. When to apply filtering Filtering is required to remove spin-induced oscillations and obtain oscillations caused solely by eccentricity. However, the procedure explained in the previous section should be applied only in the small eccentricity regime. This is because at high eccentricity, it can be challenging to distinguish between modes due to eccentric higher harmonics [70, 119, 120] (which appear as integer multiples of f_{ecc}) and the mode due to spin-induced oscillation (which appear as $f_{\text{spin}} \sim 2 - 3 \times f_{\text{ecc}}$ as we saw in figure 5). Removing higher eccentric harmonics by incorrectly identifying as spin-induced oscillation may cause significant bias in the measured eccentricity. Also, we do not require filtering at high eccentricity anyway, because the eccentric modulations become significantly larger than the spin-induced modulations.

The frequency ω_{gw} in equation (8) is the antisymmetric combination of $\omega_{2,2}^{\text{copr}}$ and $\omega_{2,-2}^{\text{copr}}$ that nearly cancels out the mode asymmetry. On the other hand, the symmetric combination of $\omega_{2,2}^{\text{copr}}$ and $\omega_{2,2}^{\text{copr}}$ [39–42],

$$\omega_+ = \frac{1}{2} (\omega_{2,2}^{\text{copr}} + \omega_{2,-2}^{\text{copr}}), \quad (14)$$

captures the mode asymmetry. Using equation (14), ω_{gw} in equation (8) can be rewritten as

$$\omega_{\text{gw}} = \omega_{2,2}^{\text{copr}} - \omega_+ \quad (15)$$

Removing the secular trend from ω_{gw} , the above equation becomes

$$\Delta\omega_{\text{gw}} = (\omega_{2,2}^{\text{copr}} - \omega_{\text{gw}}^{\text{secular}}) - \omega_+. \quad (16)$$

$$\approx (\omega_{2,2}^{\text{copr}} - \omega_{2,2}^{\text{copr,secular}}) - \omega_+, \quad (17)$$

where in equation (17) we have assumed that $\omega_{\text{gw}}^{\text{secular}} \approx \omega_{2,2}^{\text{copr,secular}}$. This is sufficient as we only need the scale of the two terms, $(\omega_{2,2}^{\text{copr}} - \omega_{2,2}^{\text{copr,secular}})$ and ω_+ , to estimate how large spin-induced effects are compared to eccentric effects. Using $\Delta\omega_{2,2}^{\text{copr}} = \omega_{2,2}^{\text{copr}} - \omega_{2,2}^{\text{copr,secular}}$, $\Delta\omega_{\text{gw}}$ can be approximately written as the sum of two contributions:

$$\Delta\omega_{\text{gw}} \approx \Delta\omega_{2,2}^{\text{copr}} - \omega_+. \quad (18)$$

In equation (18), the first term on the right contains the modulations due to eccentricity as well as spin-precession, whereas the second term is caused solely by spin-precession. For small eccentricity, $\Delta\omega_{2,2}^{\text{copr}}$ is dominated by the spin-induced effects, and becomes comparable in magnitude to ω_+ . Therefore, we use a threshold on the ratio r_{filter} , defined as the ratio of the maximum values of ω_+ and $\Delta\omega_{2,2}^{\text{copr}}$, to decide whether filtering is necessary. Since both quantities exhibit oscillations over time, we compute the average of their values at their respective local maxima (denoted by superscript “m” below),

$$r_{\text{filter}} = \frac{\overline{\omega_+}}{\overline{\Delta\omega_{2,2}^{\text{copr}}}}, \quad \bar{X} = \frac{1}{N} \sum_{i=1,\dots,N} X_i^{\text{m}}. \quad (19)$$

Both $\Delta\omega_{2,2}^{\text{copr}}$ and ω_+ oscillate in time about zero, and, hence have positive values at the local maxima, which ensures that $r_{\text{filter}} > 0$. We recommend applying the filter only if $r_{\text{filter}} > 0.2$. For smaller r_{filter} , the spin-induced oscillations are negligible compared to the eccentricity-induced oscillations, and filtering may accidentally remove higher eccentric harmonics instead, leading to bias in the measured eccentricity. In figure 6, we compare ω_+ and $\Delta\omega_{2,2}^{\text{copr}}$ for two example cases. The *left* panel shows that the amplitude of ω_+ is small compared to that of $\Delta\omega_{2,2}^{\text{copr}}$ for a system with $q = 3, \chi_p = 0.8, e_{\text{gw}} = 0.12$. For this system, $r_{\text{filter}} \approx 0.15$, and filtering ω_{gw} is not recommended. The *right* panel shows that the amplitude of ω_+ is nearly the same as the amplitude of $\Delta\omega_{2,2}^{\text{copr}}$ for a system with $q = 3, \chi_p = 0.8, e_{\text{gw}} = 0.005$. For this system, $r_{\text{filter}} \approx 0.82$ and filtering ω_{gw} is recommended.

2.8. Summary

In this section, we summarize the steps to measure eccentricity e_{gw} and mean anomaly l_{gw} given a waveform:

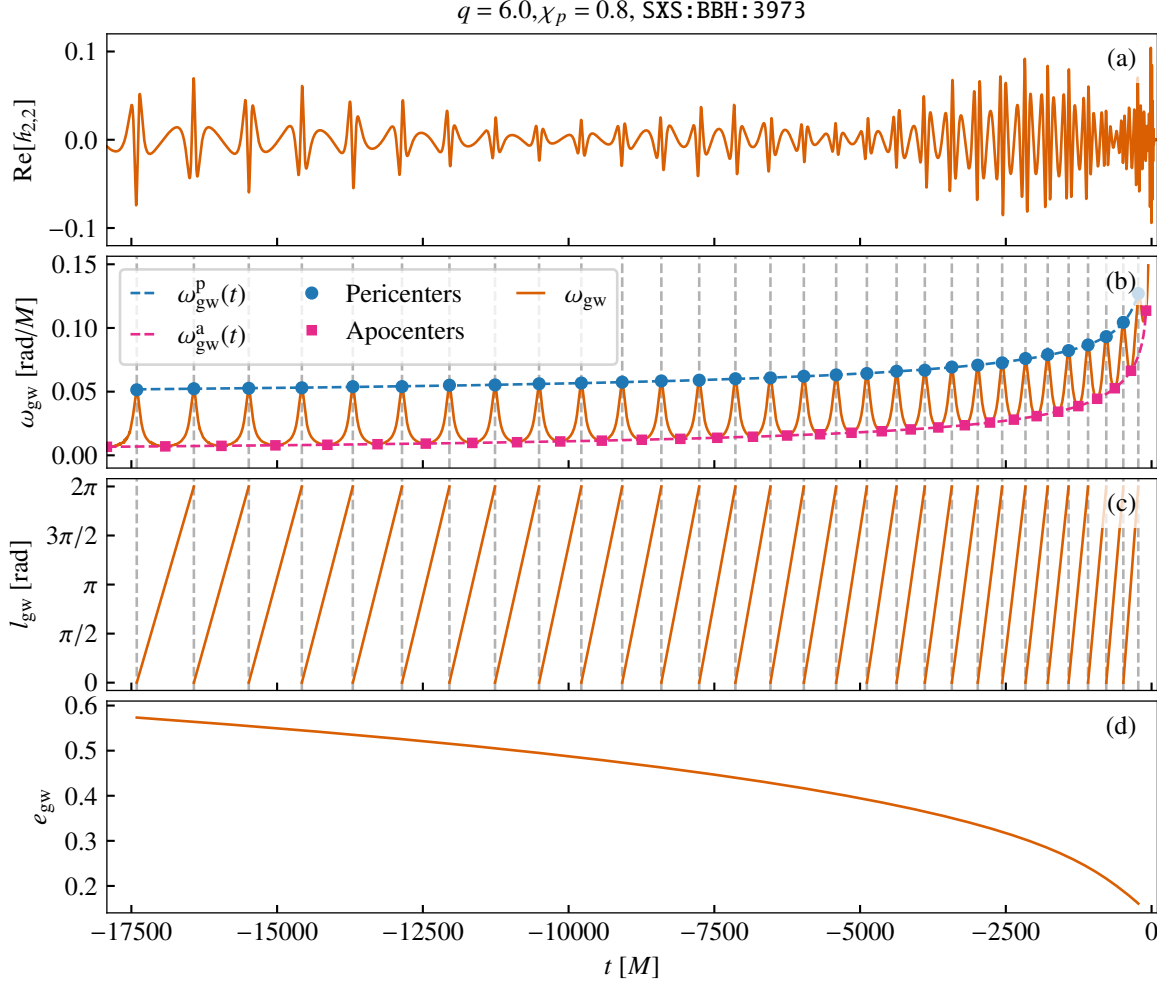


Figure 7. Demonstration of eccentricity e_{gw} and mean anomaly l_{gw} measurement for a strongly spin-precessing system. (a) Real part of the $(2, 2)$ mode in the inertial frame, showing the effects of eccentricity and spin-precession. (b) It shows the frequency ω_{gw} , antisymmetric combination of the $\omega_{2,2}^{\text{copr}}$ and $\omega_{2,-2}^{\text{copr}}$. $\omega_{\text{gw}}^{\text{p}}(t)$ and $\omega_{\text{gw}}^{\text{a}}(t)$ are the interpolants through ω_{gw} evaluated at the pericenters (blue circles) and the apocenters (pink squares), respectively. The vertical gray dashed lines denote the pericenter times. (c) Time evolution of mean anomaly l_{gw} . l_{gw} grows linearly from 0 to 2π between successive pericenters (equation (12)). (d) Time evolution of the eccentricity e_{gw} computed using equation (10) given $\omega_{\text{gw}}^{\text{p}}(t)$ and $\omega_{\text{gw}}^{\text{a}}(t)$.

- (a) If the system is spin-precessing, the waveform is transformed to the coprecessing frame. For aligned-spin systems, the inertial and coprecessing frames are equivalent.
- (b) If the waveform include memory contribution, the memory contribution is removed from the waveform before it is used for eccentricity measurement.
- (c) Instead of using only the inertial frame $(2, 2)$ mode variables, variables with reduced spin-induced oscillation, that is, A_{gw} , ϕ_{gw} and ω_{gw} provided by equation (6), (7) and (8), respectively, are used.
- (d) For small eccentricity and large spin-precession, A_{gw} and ω_{gw} are low-pass filtered to remove spin-induced oscillations. Whether filtering is required is decided using the

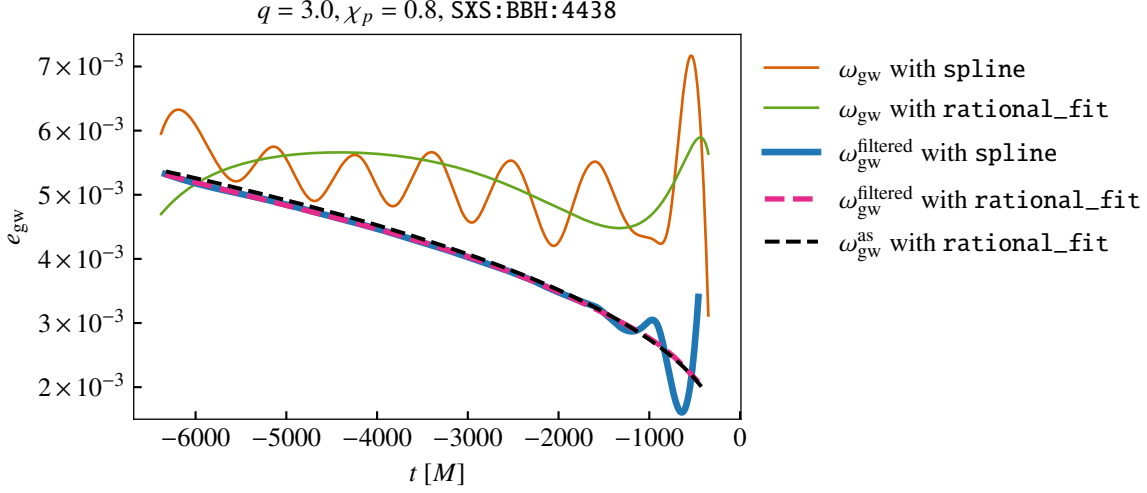


Figure 8. e_{gw} for small eccentricity and high spin-precession system SXS:BBH:4438. e_{gw} obtained using ω_{gw} without smoothing filter shows incorrect behavior (oscillates and increases near merger) which is fixed when using $\omega_{\text{gw}}^{\text{filtered}}$ with `rational_fit` for e_{gw} measurement. e_{gw} using $\omega_{\text{gw}}^{\text{filtered}}$ closely matches the $e_{\text{gw}}^{\text{as}}$ of the aligned-spin counterpart obtained using SEOBNRv5EHM. For details, see the main text.

criterion discussed in section 2.7.3.

- (e) Finally, e_{gw} and l_{gw} defined in equation (10) and (12), respectively, are computed using the GW variables computed in the previous steps. For building $\omega_{\text{gw}}^{\text{p}}(t)$ and $\omega_{\text{gw}}^{\text{a}}(t)$, using `rational_fit` (see section 2.6) is recommended over `spline` as `rational_fit` is more robust in providing consistently decreasing $e_{\text{gw}}(t)$.

Figure 7 demonstrates the computation of the eccentricity e_{gw} and the mean anomaly l_{gw} using the waveform from an NR simulation with significant spin-precession ($\chi_p = 0.8$) and large eccentricity (initial $e_{\text{gw}} \sim 0.57$). Here, we have removed the memory from the waveform, transformed the waveform to the coprecessing frame, and used `rational_fit` for building $\omega_{\text{gw}}^{\text{p}}(t)$ and $\omega_{\text{gw}}^{\text{a}}(t)$ (for this case low-pass filtering was not recommended by the criterion in section 2.7.3).

Next, we demonstrate the computation of e_{gw} for a system with significant spin-precession ($\chi_p = 0.8$) and small eccentricity (initial $e_{\text{gw}} \sim 0.005$). For this case, low-pass filtering is recommended by the criterion in section 2.7.3 to remove spin-induced oscillations from ω_{gw} and A_{gw} . In figure 8, we show how the measured $e_{\text{gw}}(t)$ varies depending on the methods used for the measurement. It contains the following cases:

- (A) ω_{gw} with `spline`: This line represents $e_{\text{gw}}(t)$ computed using `spline` interpolants with unfiltered ω_{gw} . The spin-induced modulations affect the locations of local extrema and the values of $\omega_{\text{gw}}^{\text{p}}$ and $\omega_{\text{gw}}^{\text{a}}$, which is reflected in the oscillatory behavior of e_{gw} . Additionally, note the increasing trend near the merger, which is due to the enhanced spin-induced modulation in this region. Unlike eccentric modulations, spin-induced modulations increase over time.

- (B) ω_{gw} with `rational_fit`: Same as (A), but using `rational_fit` interpolants. The small oscillations present in e_{gw} based on `spline` are gone, but the overall trend remains incorrect.
- (C) $\omega_{\text{gw}}^{\text{filtered}}$ with `spline`: Same as (A), but using $\omega_{\text{gw}}^{\text{filtered}}$. We observe that e_{gw} is monotonically decreasing for most part of its evolution except near the merger. Near the merger oscillatory behavior appears due to the use of `spline` interpolants as discussed in section 2.6 and Appendix A.
- (D) $\omega_{\text{gw}}^{\text{filtered}}$ with `rational_fit`: Same as (B), but using $\omega_{\text{gw}}^{\text{filtered}}$. Now the $e_{\text{gw}}(t)$ has expected monotonically decreasing behavior over time and does not have oscillatory behavior near the merger unlike the case for `spline`.
- (E) $\omega_{\text{gw}}^{\text{as}}$ with `rational_fit`: To assess the evolution of $e_{\text{gw}}(t)$ obtained in (D) using $\omega_{\text{gw}}^{\text{filtered}}$, we also plot $e_{\text{gw}}^{\text{as}}(t)$ from the aligned-spin counterpart using SEOBNRv5EHM [60, 61] waveform. The aligned-spin waveform is generated using the same parameters as the spin-precessing system, except for the spins, which we replace by only the z -components in the case of the aligned-spin waveform (see section 3.3 for more details). Because the waveforms in the coprecessing frame look similar to the corresponding aligned-spin waveforms, we expect that the $e_{\text{gw}}(t)$ will also look similar to the $e_{\text{gw}}^{\text{as}}(t)$ of the aligned-spin counterpart. We find that $e_{\text{gw}}^{\text{as}}(t)$ closely matches $e_{\text{gw}}(t)$, as expected, but it is necessary to use $\omega_{\text{gw}}^{\text{filtered}}$ to obtain the correct $e_{\text{gw}}(t)$.

3. Robustness checks

In this section, we check the robustness of our method of measuring eccentricity discussed in the previous section. In section 3.1, we showcase the applicability of our method on NR waveforms of different eccentricities and spin-precession. In section 3.2, we put our method to a couple of smoothness tests using a set of TEOBResumS-DaLi waveforms. In section 3.3, we compare the e_{gw} evolution of a set of spin-precessing waveforms to their aligned-spin counterpart. Finally, in section 3.4, we check the robustness of our method when applying to waveforms with small eccentricity and large spin-precession.

3.1. Applications to NR waveforms

In this section, we apply our method to compute e_{gw} from a set of NR waveforms. First, we apply it on waveforms from binary black hole systems simulated using SpEC [97]. We select four representative cases, and plot the resulting e_{gw} in figure 9: low eccentricity with aligned-spins (*top-left*), high eccentricity with aligned-spins (*top-right*), low eccentricity with high spin-precession (*bottom-left*), and high eccentricity with high spin-precession (*bottom-right*). Next, in figure 10, we repeat this for a few NR waveforms from the RIT [121–123] catalog. We select three simulations for this purpose, which contain a sufficient number of orbits for robust e_{gw} estimation ¶. The RIT simulations share the same mass ratio ($q = 1$) and spin parameters

¶ As noted in [90], this method to compute eccentricity from the waveform requires at least $\sim 4 - 5$ number of orbits. The same limitation applies in the case of spin-precessing binaries.

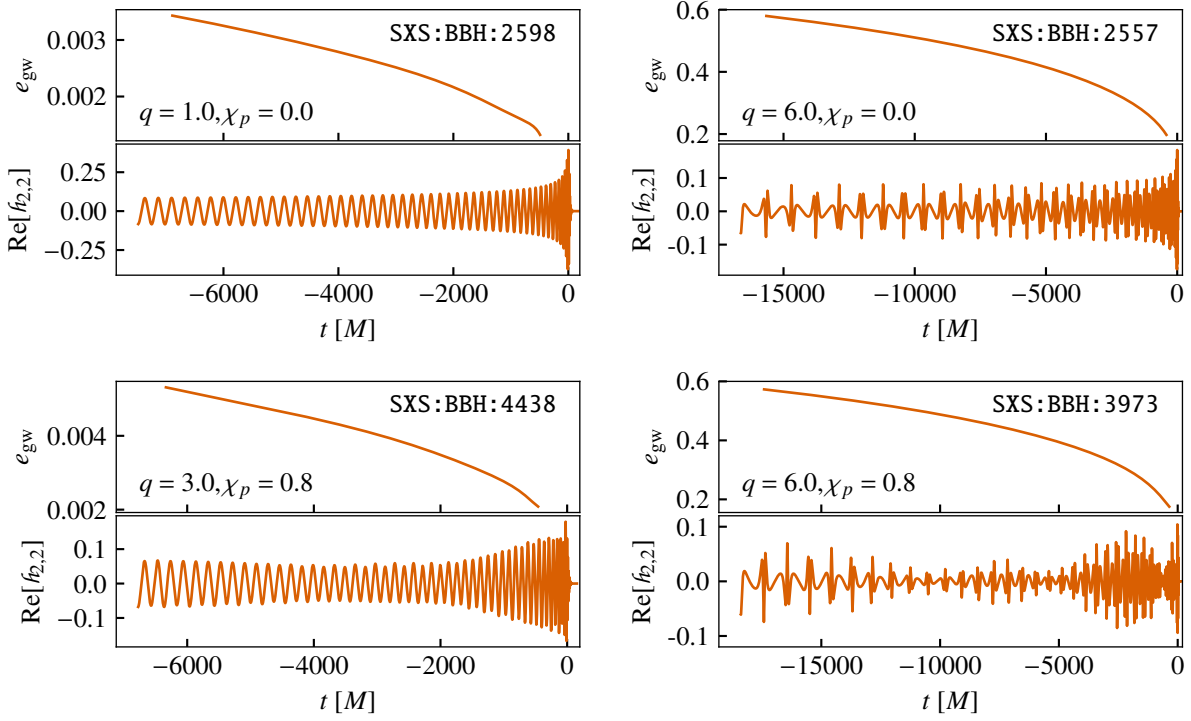


Figure 9. Application to four representative SXS waveforms obtained using SpEC. The *top* row presents aligned-spin eccentric systems, with small eccentricity on the *left* and large eccentricity on the *right*. The *bottom* row presents similar plots for spin-precessing eccentric systems—small eccentricity with high spin-precession on the *left* and high eccentricity with high spin-precession on the *right*. For each case, the *top* panel shows the e_{gw} evolution, and the *bottom* panel shows the real part of the corresponding $h_{2,2}$.

($\chi_1 = [0.7, 0, 0], \chi_2 = [0.7, 0, 0]$). In each subplot of figure 9 and figure 10, the *top* panel shows the e_{gw} evolution, while the *bottom* panel presents the real part of the corresponding $h_{2,2}$. These cases illustrate the applicability of our method to systems with varying eccentricity and spin-precession.

3.2. Smoothness tests

At present, TEOBResumS-Dalí [79, 80] is the only publicly available time-domain waveform model that supports both eccentricity and spin-precession, but it does not include mode asymmetry terms. In other words, $A_{\text{gw}}, \phi_{\text{gw}}$ and ω_{gw} are identical to the corresponding quantities from the $(2, 2)$ mode in the coprecessing frame, that is, $A_{2,2}^{\text{copr}}, \phi_{2,2}^{\text{copr}}$ and $\omega_{2,2}^{\text{copr}}$, respectively. However, unlike the NR waveforms, TEOBResumS-Dalí waveforms are not restricted to discrete points in the parameter space, and therefore, serve as a useful check of the robustness of our implementation on a larger set of waveforms. We demonstrate that our method can be applied to TEOBResumS-Dalí waveforms robustly by performing smoothness tests. As noted in [90], such smoothness tests are important not just as a robustness check of the e_{gw} measurement method, but also of the underlying waveform model.

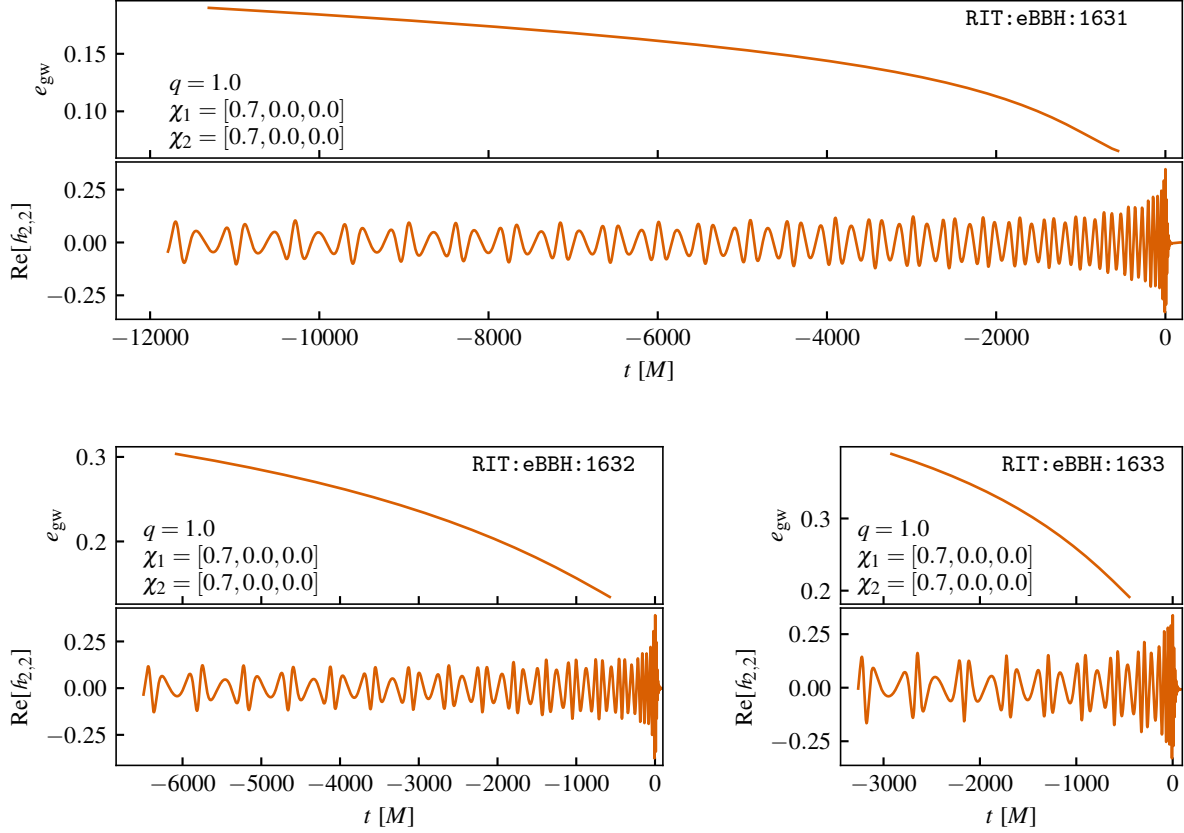


Figure 10. Application to RIT eccentric spin-precessing waveforms. For each case, the *top* panel shows the e_{gw} evolution and the *bottom* panel shows the real part of the corresponding $h_{2,2}$.

To ensure the robustness of our implementation, we put it to a couple of tests. The first test checks the relation between the measured e_{gw} and the model input eccentricity e_{eob} , and the second test checks the smoothness of the measured e_{gw} evolution. For both tests, we generate a set of 50 eccentric spin-precessing waveforms using the public waveform model `TEOBResumS-Da11` [79]. For generating this set of waveforms, we vary the initial input e_{eob} from 10^{-5} to 0.8 while keeping the mass ratio, initial input mean anomaly (l_{eob}) and spins fixed at $q = 4.0$, $l_{\text{eob}} = \pi$, $\chi_1 = \chi_2 = [0.6, 0.6, 0.3]$. We choose the initial input frequency such that the waveforms start at $t_0 \approx -20000M$.

In figure 11, the *left* panel shows the relation between the input e_{eob} at t_0 and the measured e_{gw} at \hat{t}_0 , the earliest time where e_{gw} can be measured. \hat{t}_0 is determined by $\hat{t}_0 = \max(t_0^{\text{p}}, t_0^{\text{a}})$, where t_0^{p} is the time at the first pericenter and t_0^{a} is the time at the first apocenter. For $e_{\text{eob}} \gtrsim 10^{-3}$, e_{gw} vs e_{eob} follows the $e_{\text{gw}} = e_{\text{eob}}$ line. For $e_{\text{eob}} \lesssim 10^{-3}$, e_{gw} plateaus at $\approx 10^{-3}$. This behavior was also noted in [90], and implies that the `TEOBResumS-Da11` model ceases to produce any difference in the physical content of the waveforms below $e_{\text{eob}} \lesssim 10^{-3}$. The *right* panel shows the evolution of e_{gw} . The colors represent the model input eccentricity e_{eob} at t_0 . It shows the expected monotonically decreasing trend of e_{gw} with time. All of the $e_{\text{gw}}(t)$ curves decay smoothly over time and across change of initial eccentricity, as expected. We also note that for

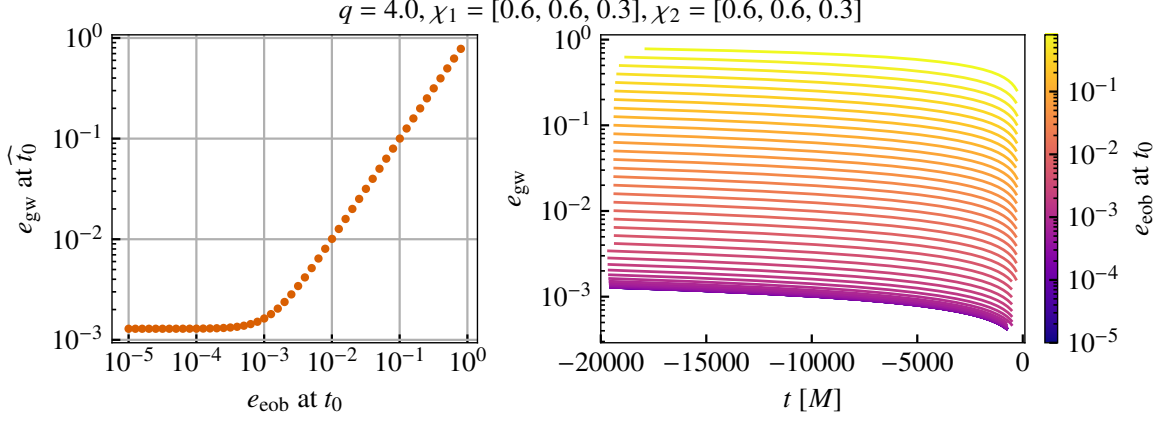


Figure 11. Smoothness tests. *Left:* e_{gw} vs e_{eob} smoothness test. The y -axis represents the eccentricity e_{gw} at the earliest time \hat{t}_0 and the x -axis represents the input model eccentricity e_{eob} at $t_0 = -20000M$. The measured eccentricity and the input model eccentricity follows the $e_{\text{gw}} = e_{\text{eob}}$ line for $e_{\text{eob}} \gtrsim 10^{-3}$. For $e_{\text{eob}} \lesssim 10^{-3}$, e_{gw} becomes constant implying that the physical content of the waveform stops changing even though the model input eccentricity e_{eob} keeps changing. *Right:* e_{gw} vs t smoothness test. The colors represent the initial eccentricity e_{eob} at t_0 used as an input to TEOBResumS-Dalí. e_{eob} varies from 10^{-5} to 0.8. We choose the starting frequency such that the waveforms start at $t_0 \approx -20000M$.

$e_{\text{eob}} \lesssim 10^{-3}$, the $e_{\text{gw}}(t)$ curves overlap with each other, for the same reason noted above.

3.3. Comparison to aligned-spin counterpart

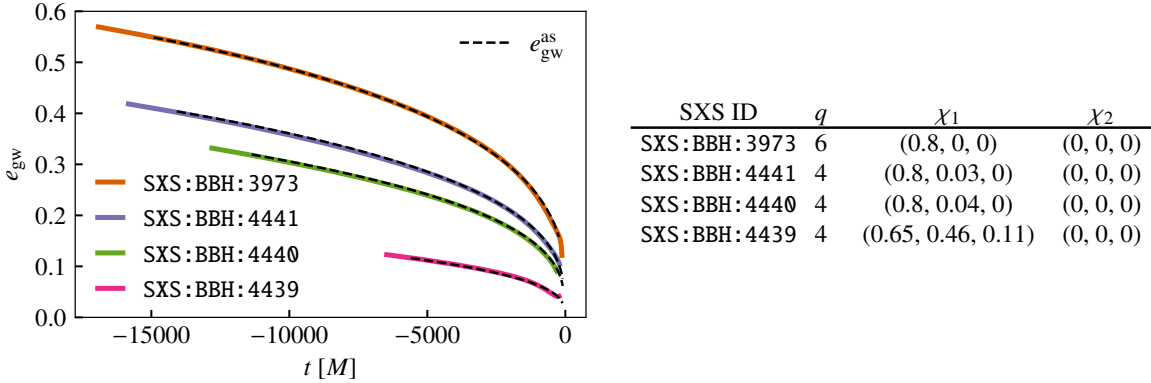


Figure 12. e_{gw} vs $e_{\text{gw}}^{\text{as}}$ for eccentric spin-precessing NR waveforms from the SXS Collaboration. The solid lines represent the e_{gw} evolution for different NR simulations with varying initial eccentricity. For each of these lines, the corresponding $e_{\text{gw}}^{\text{as}}$ is shown using dashed line. $e_{\text{gw}}^{\text{as}}$ is obtained using SEOBNRv5EHM model with the same mass ratio and z -components of the spins. The eccentricity parameters ($e_{\text{gw}}, l_{\text{gw}}$), at a reference frequency f_{ref} corresponding to the second pericenter, are estimated first from the NR waveform, and then used as an input to SEOBNRv5EHM.

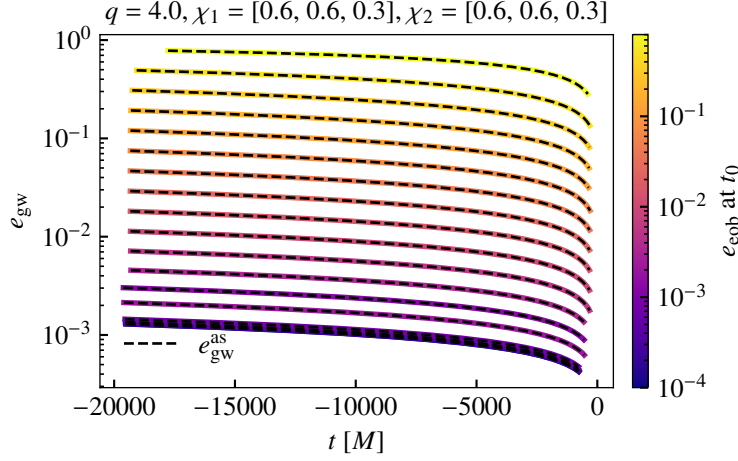


Figure 13. e_{gw} vs $e_{\text{gw}}^{\text{as}}$ for TEOBResumS-Dalí. Same as figure 12, but here we use TEOBResumS-Dalí to show the comparison for a larger set of waveforms with initial e_{eob} in $[10^{-4}, 0.8]$. In this case, the input parameters for the spin-precessing and the aligned-spin waveforms are the same, except that for the aligned-spin case, only z components of the spins are non-zero. The colorbar shows the initial input e_{eob} at the starting time $t_0 \approx -20000M$.

For computing $e_{\text{gw}}(t)$ of a spin-precessing system, the waveform is transformed to the coprecessing frame. This transformation removes most of the spin-precession effects from the waveform, making them similar to those of an aligned-spin system. Therefore, we expect the measured $e_{\text{gw}}(t)$ to also look similar to the eccentricity $e_{\text{gw}}^{\text{as}}$ of its aligned-spin counterpart. The waveform of the aligned-spin counterpart is generated using the same parameters as the spin-precessing system, except that the spins are replaced by only the z -components (χ_{1z}, χ_{2z}). We find that e_{gw} and the eccentricity of its aligned-spin counterpart, $e_{\text{gw}}^{\text{as}}$, are very close to each other as expected.

First we perform this on a set of eccentric spin-precessing NR simulations (see [72] for further details on these simulations) performed using SpEC [97]. Because the NR simulations are performed at discrete points in the binary's parameter space, it is difficult to find the aligned-spin counterpart from the existing NR catalog. Instead, in this case, we generate the aligned-spin counterpart using the SEOBNRv5EHM model [60, 61]. As an input for the model, we use the same mass ratio and z -components of the spins (χ_{1z}, χ_{2z}) as the NR spin-precessing waveform. For the eccentricity parameters, we first compute the eccentricity e_{gw} and mean anomaly l_{gw} at the earliest dimensionless frequency f_{ref}^+ , after removing 2 orbits* of data from the initial part of the waveform as junk radiation. Then we use these as the input initial eccentricity and mean anomaly to the SEOBNRv5EHM model for generating the aligned-spin waveform. In figure 12, we plot $e_{\text{gw}}(t)$ for the four NR waveforms with varying

⁺ f_{ref} is related to reference time t_{ref} , where $(e_{\text{gw}}, l_{\text{gw}})$ is computed, by the equation $\langle \omega_{\text{gw}} \rangle(t_{\text{ref}}) = 2\pi f_{\text{ref}}$, where $\langle \omega_{\text{gw}} \rangle$ is the orbit averaged ω_{gw} . See section II.E in [90] for more details, where it is discussed for aligned-spin systems, but applies to spin-precessing systems as well by working with ω_{gw} , instead of ω_{22} .

* One orbit is approximated as a phase difference of 2π in the orbital phase, which is computed from the black hole trajectories provided along with the simulation data.

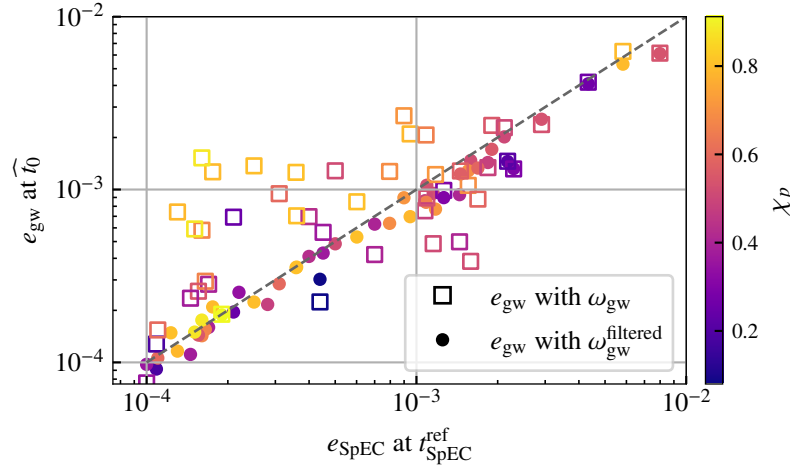


Figure 14. e_{gw} at \hat{t}_0 vs e_{SpEC} at $t_{\text{SpEC}}^{\text{ref}}$ for spin-precessing systems with $10^{-4} \lesssim e_{\text{gw}} \lesssim 10^{-2}$. Due to spin-induced effects dominating over eccentric effects, e_{gw} measured using unfiltered ω_{gw} can differ from the corresponding e_{SpEC} values by a factor of ~ 10 for $e_{\text{SpEC}} \lesssim 10^{-3}$. For the same cases, when using $\omega_{\text{gw}}^{\text{filtered}}$, e_{gw} and e_{SpEC} agrees within a factor of ~ 2 . The colors represent the initial values of χ_p . One can see that, in general, with increasing χ_p , filtering becomes more important in the small eccentricity regime.

initial eccentricity. The corresponding $e_{\text{gw}}^{\text{as}}(t)$ of the aligned-spin counterpart is shown using the dashed lines.

Next, we do the same study using the TEOBResumS-Dalí model. In this case, we can generate the aligned-spin counterpart using the exact set of input parameters (mass ratio, eccentricity, mean anomaly and the z -component of the spin vectors) as the spin-precessing one. Also, we can generate a larger set of waveforms with TEOBResumS-Dalí. In figure 13, we plot the $e_{\text{gw}}(t)$ for 20 TEOBResumS-Dalí waveforms with $q = 4, \chi_1 = \chi_2 = [0.6, 0.6, 0.3]$ and initial e_{cob} varying from 10^{-4} to $e_{\text{cob}} = 0.8$. We choose the starting frequencies so that the resulting waveforms start at $t_0 \approx -20000M$. The input initial e_{cob} are shown using the colorbar. The dashed lines represent the eccentricity $e_{\text{gw}}^{\text{as}}(t)$ of the aligned-spin counterpart for each of these waveforms.

These checks serve two purposes: First, they demonstrate the robustness of our method in measuring e_{gw} from spin-precessing waveforms, as $e_{\text{gw}}^{\text{as}}$ measured from the aligned-spin counterpart serves as a useful reference. Second, even though the association of an aligned-spin counterpart to a spin-precessing system is only approximate, these checks demonstrate that the approach of frame-twisting an aligned-spin waveform to approximate a spin-precessing waveform can be a reasonable waveform modeling strategy even in the eccentric regime (see [79] for work in this direction).

3.4. Applicability in the small eccentricity & large spin-precession regime

In section 2.7, we discussed how spin-induced effects may become non-negligible compared to the eccentric modulations in the small eccentricity and large spin-precession limit, and

provided a method based on low-pass filtering, to remove the spin-induced modulations. In this section, we check the robustness of this method by applying it to a set of 50 spin-precessing simulations from the SXS catalog [96] with $10^{-4} \lesssim e_{\text{SpEC}} \lesssim 10^{-2}$. A list of these simulations are provided in table C1 in Appendix C.

In figure 14, we plot the e_{gw} at \hat{t}_0 vs e_{SpEC} at $t_{\text{SpEC}}^{\text{ref}}$ for this set of simulations, where $t_{\text{SpEC}}^{\text{ref}}$ is the reference time where e_{SpEC} is measured in the SpEC metadata. All of the cases in the figure have $r_{\text{filter}} > 0.2$, and therefore, we apply the low-pass filter to ω_{gw} . Note that the e_{gw} measured using $\omega_{\text{gw}}^{\text{filtered}}$ is consistent with e_{SpEC} within a factor of ~ 2 . The absolute difference is of the order of e_{SpEC} . On the other hand, the e_{gw} measured using ω_{gw} without applying filtering shows a significant deviation as e_{SpEC} goes below 10^{-3} , and e_{gw} can differ from e_{SpEC} by a factor of ~ 10 . Note that e_{SpEC} is computed from the black hole trajectories by fitting the first derivative of the orbital frequency [96], whereas e_{gw} is computed using ω_{gw} from the GW waveforms. Also, e_{SpEC} is only meant to be an approximate estimate of the eccentricity, and should be treated only as a reference [96]. Nevertheless, it serves as a useful check for the filtering method.

4. Conclusion

We present a generalized definition of eccentricity, e_{gw} , and mean anomaly, l_{gw} , for compact binaries on generic bound orbits that exhibit both eccentricity and spin-precession. Spin-precession adds two complexities in the eccentricity measurement from GW waveforms — precession of the orbital plane about the total angular momentum of the system, and the mode asymmetry between positive and negative m modes. The precession of the orbital plane causes leakage of GW power from the $(\ell = 2, m = \pm 2)$ modes into $(\ell = 2, m \neq 2)$. To fix this, following previous works [45–51, 79], we transform the waveforms to the coprecessing frame, and reestablish the mode hierarchy where the $(\ell = 2, m = \pm 2)$ modes remain the dominant modes during the entire inspiral. However, even in the coprecessing frame, the mode asymmetry causes nonmonotonicity in the values of the $(2, 2)$ mode frequency at the extrema. To address this, following previous works [39–42], instead of using only the $(2, 2)$ mode, we use amplitude A_{gw} and phase ϕ_{gw} defined by the symmetric and anti-symmetric combination of the amplitudes and phases, respectively, of the $(2, 2)$ and $(2, -2)$ modes in the coprecessing frame. We then use A_{gw} , ϕ_{gw} , and ω_{gw} (the first time derivative of ϕ_{gw}) to define the eccentricity e_{gw} and mean anomaly l_{gw} .

To ensure the monotonicity of $e_{\text{gw}}(t)$, we also adopted an interpolation method, `rational_fit`, for building the interpolants $\omega_{\text{gw}}^{\text{p}}(t)$ and $\omega_{\text{gw}}^{\text{a}}(t)$ for ω_{gw} values at the pericenters and the apocenters, respectively, using rational function approximation. We find `rational_fit` to be highly robust and better than the Spline based method, `spline`, in capturing the trend of e_{gw} near the merger and avoiding small numerical noise that might be present in the waveform data.

We find our definition of eccentricity using A_{gw} , ϕ_{gw} and ω_{gw} to be robust in measuring eccentricity for highly spin-precessing systems. We demonstrated its robustness by applying it to NR as well as TEOBResumS–Dali waveforms. We also performed smoothness tests by

plotting — (a) e_{gw} at initial time vs initial model input eccentricity e_{cob} , and (b) the evolution of e_{gw} over time — for a large set of spin-precessing TEOBResumS-Da11 waveforms with the model input eccentricity varying from $e_{\text{cob}} = 10^{-5}$ to $e_{\text{cob}} = 0.8$.

For small eccentricity ($e_{\text{gw}} \lesssim 10^{-2}$) and high spin-precession ($\chi_p \approx 0.8$), spin-induced modulations due to mode asymmetry may become non-negligible compared to eccentric modulations. We provide robust method based on low-pass filtering to remove such spin-induced oscillations. We find that the spin-induced modulation oscillate at a timescale about 2-3 times the timescale of the eccentric modulations. We utilize this difference in the timescale of these two effects to build a consistent strategy for removing the spin-induced modulation by applying a low-pass filter.

The spin-induced modulations appear only in NR waveforms since the currently available eccentric waveform models [76, 78–80] do not contain mode asymmetry. However, in the future, we expect waveform models to include terms arising from mode asymmetry. In that case, spin-induced oscillations will appear in both ω_{gw} and A_{gw} . While the method described in section 2.7 can be used to remove these oscillations, waveform models will offer a more direct approach by giving us full control over the mode asymmetry terms. Specifically, we can suppress the spin-induced oscillations by disabling these terms when generating waveforms for the purpose of measuring e_{gw} . Moreover, such models could be used to remove spin-induced oscillations from NR waveforms by constructing an approximate model for these effects. We leave these possibilities for future work, once eccentric waveform models incorporating mode asymmetry become available.

Python implementation of our methods is publicly available via package `gw_eccentricity` [90].

Acknowledgments

The authors thank Keefe Mitman, Rossella Gamba for valuable comments on the draft, and Aldo Gamboa and Leo C. Stein for useful discussion. M.A.S.’s research was partially supported by the National Research Foundation of Korea under grant No. NRF-2021R1A2C2012473. V.V. acknowledges support from NSF Grant No. PHY-2309301 and UMass Dartmouth’s Marine and Undersea Technology (MUST) Research Program funded by the Office of Naval Research (ONR) under Grant No. N00014-23-1-2141. A. Ramos-Buades is supported by the Veni research programme which is (partly) financed by the Dutch Research Council (NWO) under the grant VI.Veni.222.396; acknowledges support from the Spanish Agencia Estatal de Investigación grant PID2022-138626NB-I00 funded by MICIU/AEI/10.13039/501100011033 and the ERDF/EU; is supported by the Spanish Ministerio de Ciencia, Innovación y Universidades (Beatriz Galindo, BG23/00056) and co-financed by UIB. L. E. Kidder’s work was supported by the National Science Foundation under Grants No. PHY-2407742, No. PHY-2207342, and No. OAC-2209655, and by the Sherman Fairchild Foundation at Cornell. This material is based upon work supported by National Science Foundation’s (NSF) LIGO Laboratory which is a major facility fully funded by the NSF. Part of the numerical calculations reported in this paper, as well as the development of `gw_eccentricity` [90], were carried

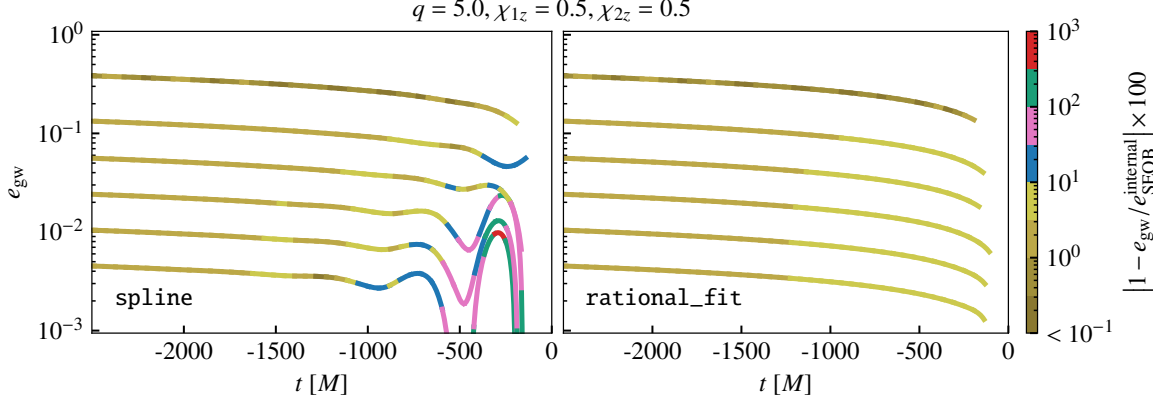


Figure A1. Comparison of e_{gw} measurements using two interpolation methods for $\omega_{\text{gw}}^{\text{p}}(t)$ and $\omega_{\text{gw}}^{\text{a}}(t)$. *Left:* e_{gw} computed using the spline interpolants for $\omega_{\text{gw}}^{\text{p}}(t)$ and $\omega_{\text{gw}}^{\text{a}}(t)$. *Right:* presents the same using the rational_fit method. In both panels, the colors indicate the instantaneous percentage difference $|1 - e_{\text{gw}}/e_{\text{SEOB}}^{\text{internal}}|$ between e_{gw} and $e_{\text{SEOB}}^{\text{internal}}$, where $e_{\text{SEOB}}^{\text{internal}}$ is the eccentricity defined internally by SEOBNRv5EHM. The rational_fit method demonstrates consistently reduced oscillations in e_{gw} compared to the spline method. As a result, the maximum difference between $e_{\text{SEOB}}^{\text{internal}}$ and e_{gw} remains below 10% with rational_fit, whereas it can reach up to $\sim 1000\%$ when using spline, especially for small eccentricities ($e_{\text{gw}} \lesssim 5 \times 10^{-2}$) and near the merger. $e_{\text{gw}}(t)$ in this figure are computed using ResidualAmplitude method.

out on the Alice cluster at the International Centre for Theoretical Sciences, Tata Institute of Fundamental Research.

Appendix A. Rational Fit vs Spline

In section 2.6, we discussed why rational_fit is a better choice when building the $\omega_{\text{gw}}^{\text{p}}(t)$ and $\omega_{\text{gw}}^{\text{a}}(t)$ interpolants compared to using spline. In this section, we study the robustness of these two methods by applying them on a set of aligned-spin waveforms generated using SEOBNRv5EHM [60, 61] with eccentricity varying from $e_{\text{eob}} \gtrsim 10^{-3}$ to $e_{\text{eob}} = 0.8$ $\#$. To check the robustness, we compare the measured e_{gw} to $e_{\text{SEOB}}^{\text{internal}}$ defined within the EOB dynamics in SEOBNRv5EHM using PN expressions.

In figure A1, we plot e_{gw} using spline on the left panel and the same using rational_fit on the right panel. In both the panels, the colors represent the instantaneous percentage difference $|1 - e_{\text{gw}}/e_{\text{SEOB}}^{\text{internal}}|$. Similar to figure 4, the difference is small for regions far from the merger, and are of the same order for both spline and rational_fit. However, close to the merger, spline shows larger relative difference due to the oscillations introduced by spline. On the other hand, the e_{gw} is consistently monotonic in case of rational_fit. The maximum difference with respect to $e_{\text{SEOB}}^{\text{internal}}$ over the set of these waveforms is orders of magnitude smaller for rational_fit (maximum differences fall below $\sim 10\%$) compared

$\#$ We restrict the upper limit for e_{eob} to 0.8. For $e_{\text{eob}} \gtrsim 0.8$, we find $e_{\text{SEOB}}^{\text{internal}}$ to become oscillatory for the initial values used in the test. See section IV.E in [61] for the domain of robustness ($e_{\text{eob}} \lesssim 0.7$) of SEOBNRv5EHM.

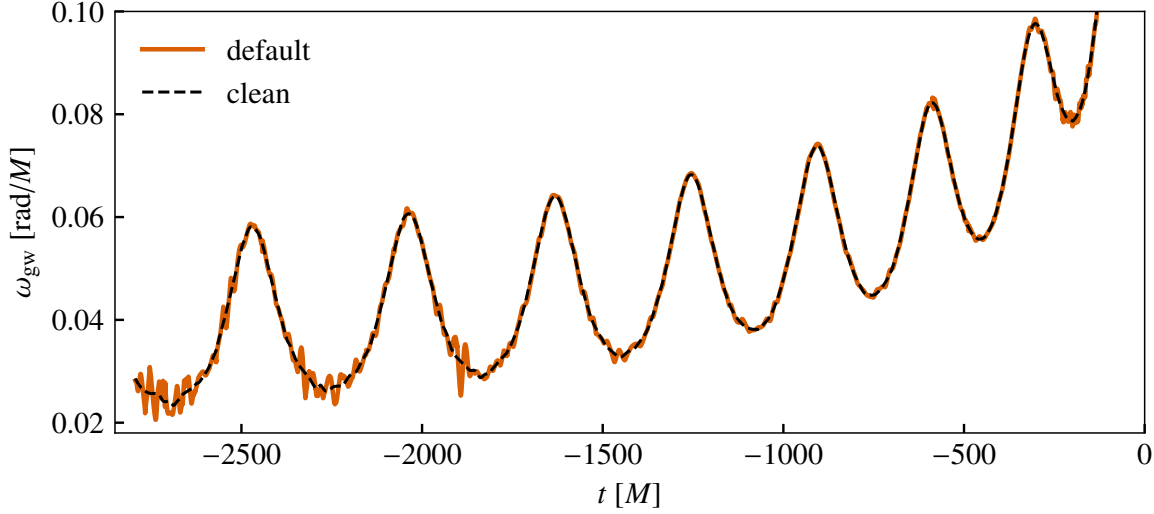


Figure B1. Numerical noise in ω_{gw} (solid line) from SXS:BBH:1370. The dashed line is obtained by applying Savitzky-Golay [125] filter implemented as `savgol_filter` in `scipy.signal`.

to `spline` (maximum differences reach up to $\sim 1000\%$), especially for small eccentricities ($e_{\text{gw}} \lesssim 5 \times 10^{-2}$) and near the merger.

Appendix B. Eccentricity measurement in presence of numerical noise

One needs to be careful when measuring eccentricity from waveforms containing numerical noise, for example, obtained using NR simulations. Recently it was highlighted in [93] (e.g., see their figure 3) that when computing e_{gw} with `spline` on a set of non-spinning eccentric NR waveforms from [124], the $e_{\text{gw}}(t)$ curves, for a few cases, exhibit oscillations. In this section, we argue that the oscillations showed in [93] are driven mainly by the numerical noise in the waveforms.

We consider 19 SXS waveforms from [124]. This is the same set of simulations used in [93], except that we have excluded SXS:BBH:1363, which has been deprecated in the latest SXS catalog [96], and included SXS:BBH:1374, which was not used in [93]. To illustrate the numerical noise present in the waveforms, we take a representative simulation SXS:BBH:1370 ($q = 2$), and plot the corresponding ω_{gw} (solid line, referred to as “default”) in figure B1, where one can see the presence of numerical noise. These numerical noise in ω_{gw} can be removed using a filter such as the Savitzky-Golay filter [125], which is available as `savgol_filter` in `scipy.signal`. The dashed line (referred to as “clean”) in figure B1 shows the ω_{gw} after removing the noise using `savgol_filter`.

In figure B2, we plot $e_{\text{gw}}(t)$ for the 19 SXS waveforms mentioned above. The *top-left* panel shows $e_{\text{gw}}(t)$ measured using `spline`, which exhibits oscillations similar to those reported in [93]. The oscillations in the earlier times are caused by numerical noise present in the waveforms (as shown in figure B1 for a case corresponding to the $e_{\text{gw}}(t)$ highlighted in dark),

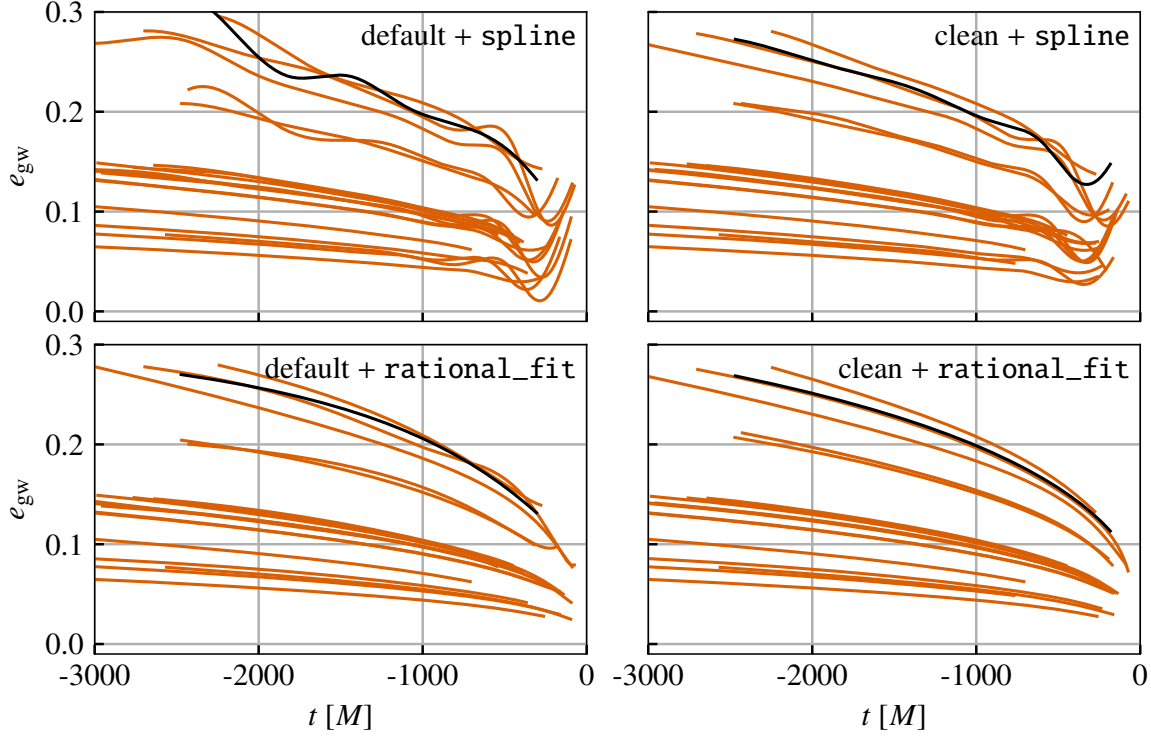


Figure B2. e_{gw} measurement of 19 SXS waveforms from [124]. *Top-left:* $e_{\text{gw}}(t)$ using `spline` without filtering out the numerical noise from the waveforms. The numerical noise affect the interpolants built using `spline`. *Top-right:* $e_{\text{gw}}(t)$ using `spline` after filtering out the numerical noise from the waveforms. The oscillations in the early parts, seen in the *top-left* panel, are gone. *Bottom-left:* $e_{\text{gw}}(t)$ using `rational_fit` without filtering out the numerical noise from the waveforms. Oscillations in $e_{\text{gw}}(t)$, seen in *top-left* panel, are mostly removed. This is because `rational_fit` is less sensitive to small numerical noise. *Bottom-right:* $e_{\text{gw}}(t)$ using `rational_fit` after filtering out the numerical noise from the waveforms. $e_{\text{gw}}(t)$ does not show any visible oscillations. The black curve in each panel represents a case (SXS:BBH:1370) where the waveform contains numerical noise, as shown in figure B1.

whereas the oscillations close to merger are due to limitation of `spline` method. The fact that the numerical noise is the main reason behind the oscillations in the early parts is evident when we apply `savgol_filter` to remove the noise from the waveforms. In the *top-right* panel, we plot $e_{\text{gw}}(t)$ with `spline` after removing numerical noise from the waveforms. Note that there are no oscillations in the early part of $e_{\text{gw}}(t)$. There are still oscillations near the merger, which we expect when using `spline` from our discussion in section 2.6 and Appendix A.

Next, we explore how $e_{\text{gw}}(t)$ behaves when using `rational_fit` instead of `spline`. In the *bottom-left* panel of figure B2, we plot $e_{\text{gw}}(t)$ using `rational_fit` without removing the numerical noise from the waveforms. We note that, unlike $e_{\text{gw}}(t)$ in *top-left* panel where `spline` was used, $e_{\text{gw}}(t)$ in the *bottom-left* panel exhibit significantly lower oscillations. This can be attributed to the fact that `rational_fit` is less sensitive to small numerical noise than `spline`. Finally, in the *bottom-right* panel, we plot $e_{\text{gw}}(t)$ using `rational_fit` with the numerical noise removed from the waveforms, where no visible oscillations are noted.

To summarize, when working with NR waveforms, it is important to account for numerical noise, especially when working with quantities like the GW frequency (which is used to define e_{gw}). While using `rational_fit` can help reduce the artificial oscillations in $e_{\text{gw}}(t)$ caused by such noise, it may not be sufficient if the noise level is high. Therefore, for a smooth and monotonic $e_{\text{gw}}(t)$, we recommend both using `rational_fit` and applying appropriate noise removal. Since a one-size-fits-all filtering approach is unlikely to effectively handle varying levels of numerical noise across different waveforms, we leave the task of noise removal to the user, but provide diagnostic plots within `gw_eccentricity` [90] for quantities such as ω_{gw} to guide the user [126].

Appendix C. SXS simulations used in figure 14

Table C1. List of simulations from the SXS catalog [96] used in figure 14 for robustness check in the small eccentricity regime.

SXS:BBH:0163	SXS:BBH:1284	SXS:BBH:1344	SXS:BBH:3053	SXS:BBH:3435
SXS:BBH:0316	SXS:BBH:1291	SXS:BBH:1383	SXS:BBH:3153	SXS:BBH:3463
SXS:BBH:0761	SXS:BBH:1298	SXS:BBH:1384	SXS:BBH:3232	SXS:BBH:3516
SXS:BBH:0846	SXS:BBH:1304	SXS:BBH:1867	SXS:BBH:3357	SXS:BBH:3517
SXS:BBH:1004	SXS:BBH:1305	SXS:BBH:2191	SXS:BBH:3358	SXS:BBH:3523
SXS:BBH:1104	SXS:BBH:1314	SXS:BBH:2685	SXS:BBH:3363	SXS:BBH:4037
SXS:BBH:1109	SXS:BBH:1322	SXS:BBH:2811	SXS:BBH:3372	SXS:BBH:4053
SXS:BBH:1239	SXS:BBH:1327	SXS:BBH:2828	SXS:BBH:3380	SXS:BBH:4074
SXS:BBH:1252	SXS:BBH:1329	SXS:BBH:2859	SXS:BBH:3390	SXS:BBH:4153
SXS:BBH:1266	SXS:BBH:1341	SXS:BBH:2970	SXS:BBH:3416	SXS:BBH:4438

References

- [1] Aasi J *et al.* (LIGO Scientific) 2015 *Class. Quant. Grav.* **32** 074001 [arXiv:1411.4547]
- [2] Acernese F *et al.* (Virgo) 2015 *Class. Quant. Grav.* **32** 024001 [arXiv:1408.3978]
- [3] Akutsu T *et al.* (KAGRA) 2021 *PTEP* **2021** 05A101 [arXiv:2005.05574]
- [4] LIGO Scientific Collaboration and Virgo Collaboration 2018 GWTC-1 <https://doi.org/10.7935/82H3-HH23>
- [5] LIGO Scientific Collaboration and Virgo Collaboration 2020 GWTC-2 <https://doi.org/10.7935/99gf-ax93>
- [6] Abbott R *et al.* (LIGO Scientific, VIRGO) 2024 *Phys. Rev. D* **109** 022001 [arXiv:2108.01045]
- [7] Abbott R *et al.* (KAGRA, VIRGO, LIGO Scientific) 2023 *Phys. Rev. X* **13** 041039 [arXiv:2111.03606]
- [8] Mapelli M 2020 *Frontiers in Astronomy and Space Sciences* **7** 38 [arXiv:2105.12455]
- [9] Mandel I and Farmer A 2022 *Phys. Rept.* **955** 1–24 [arXiv:1806.05820]
- [10] Samsing J 2018 *Phys. Rev. D* **97** 103014 [arXiv:1711.07452]
- [11] Zevin M, Samsing J, Rodriguez C, Haster C J and Ramirez-Ruiz E 2019 *Astrophys. J.* **871** 91 [arXiv:1810.00901]
- [12] Antonini F and Rasio F A 2016 *Astrophys. J.* **831** 187 [arXiv:1606.04889]
- [13] Samsing J, Bartos I, D’Orazio D J, Haiman Z, Kocsis B, Leigh N W C, Liu B, Pessah M E and Tagawa H 2022 *Nature* **603** 237–240 [arXiv:2010.09765]
- [14] Tagawa H, Kocsis B, Haiman Z, Bartos I, Omukai K and Samsing J 2021 *Astrophys. J. Lett.* **907** L20 [arXiv:2010.10526]

- [15] Peters P C and Mathews J 1963 *Phys. Rev.* **131** 435–439
- [16] Peters P C 1964 *Phys. Rev.* **136** B1224–B1232
- [17] Naoz S 2016 *Annual Review of Astronomy and Astrophysics* **54** 441–489 [arXiv:1601.07175]
- [18] Antonini F, Toonen S and Hamers A S 2017 *Astrophys. J.* **841** 77 [arXiv:1703.06614]
- [19] Randall L and Xianyu Z Z 2018 *Astrophys. J.* **853** 93 [arXiv:1708.08569]
- [20] Yu H, Ma S, Giesler M and Chen Y 2020 *Phys. Rev. D* **102** 123009 [arXiv:2007.12978]
- [21] Apostolatos T A, Cutler C, Sussman G J and Thorne K S 1994 *Phys. Rev. D* **49**(12) 6274–6297 <https://link.aps.org/doi/10.1103/PhysRevD.49.6274>
- [22] Kidder L E 1995 *Phys. Rev. D* **52** 821–847 [arXiv:gr-qc/9506022]
- [23] Favata M, Kim C, Arun K G, Kim J and Lee H W 2022 *Phys. Rev. D* **105** 023003 [arXiv:2108.05861]
- [24] Islam T, Varma V, Lodman J, Field S E, Khanna G, Scheel M A, Pfeiffer H P, Gerosa D and Kidder L E 2021 *Phys. Rev. D* **103** 064022 [arXiv:2101.11798]
- [25] O’Shea E and Kumar P 2023 *Phys. Rev. D* **108** 104018 [arXiv:2107.07981]
- [26] Clarke T A, Romero-Shaw I M, Lasky P D and Thrane E 2022 *Mon. Not. Roy. Astron. Soc.* **517** 3778–3784 [arXiv:2206.14006]
- [27] Ramos-Buades A, Buonanno A and Gair J 2023 [arXiv:2309.15528]
- [28] Dutta Roy P and Saini P 2024 *Phys. Rev. D* **110** 024002 [arXiv:2403.02404]
- [29] Nee P J *et al.* 2025 [arXiv:2503.05422]
- [30] Huez G, Bernuzzi S, Breschi M and Gamba R 2025 [arXiv:2504.18622]
- [31] Narayan P, Johnson-McDaniel N K and Gupta A 2023 *Phys. Rev. D* **108** 064003 [arXiv:2306.04068]
- [32] Shaikh M A, Bhat S A and Kapadia S J 2024 *Phys. Rev. D* **110** 024030 [arXiv:2402.15110]
- [33] Gupta A *et al.* 2024 [arXiv:2405.02197]
- [34] Pan Y, Buonanno A, Taracchini A, Kidder L E, Mroué A H, Pfeiffer H P, Scheel M A and Szilágyi B 2014 *Phys. Rev. D* **89** 084006 [arXiv:1307.6232]
- [35] Hannam M, Schmidt P, Bohé A, Haegel L, Husa S, Ohme F, Pratten G and Pürrer M 2014 *Phys. Rev. Lett.* **113** 151101 [arXiv:1308.3271]
- [36] Taracchini A *et al.* 2014 *Phys. Rev. D* **89** 061502 [arXiv:1311.2544]
- [37] Babak S, Taracchini A and Buonanno A 2017 *Phys. Rev. D* **95** 024010 [arXiv:1607.05661]
- [38] Khan S, Chatziioannou K, Hannam M and Ohme F 2019 *Phys. Rev. D* **100** 024059 [arXiv:1809.10113]
- [39] Boyle M, Kidder L E, Ossokine S and Pfeiffer H P 2014 [arXiv:1409.4431]
- [40] Blackman J, Field S E, Scheel M A, Galley C R, Ott C D, Boyle M, Kidder L E, Pfeiffer H P and Szilágyi B 2017 *Phys. Rev. D* **96** 024058 [arXiv:1705.07089]
- [41] Blackman J, Field S E, Scheel M A, Galley C R, Hemberger D A, Schmidt P and Smith R 2017 *Phys. Rev. D* **95** 104023 [arXiv:1701.00550]
- [42] Varma V, Field S E, Scheel M A, Blackman J, Gerosa D, Stein L C, Kidder L E and Pfeiffer H P 2019 *Phys. Rev. Research* **1** 033015 [arXiv:1905.09300]
- [43] Pratten G *et al.* 2021 *Phys. Rev. D* **103** 104056 [arXiv:2004.06503]
- [44] Ossokine S *et al.* 2020 *Phys. Rev. D* **102** 044055 [arXiv:2004.09442]
- [45] Akçay S, Gamba R and Bernuzzi S 2021 *Phys. Rev. D* **103** 024014 [arXiv:2005.05338]
- [46] Gamba R, Akçay S, Bernuzzi S and Williams J 2022 *Phys. Rev. D* **106** 024020 [arXiv:2111.03675]
- [47] Estellés H, Ramos-Buades A, Husa S, García-Quirós C, Colleoni M, Haegel L and Jaume R 2021 *Phys. Rev. D* **103** 124060 [arXiv:2004.08302]
- [48] Estellés H, Husa S, Colleoni M, Keitel D, Mateu-Lucena M, García-Quirós C, Ramos-Buades A and Borchers A 2022 *Phys. Rev. D* **105** 084039 [arXiv:2012.11923]
- [49] Estellés H, Colleoni M, García-Quirós C, Husa S, Keitel D, Mateu-Lucena M, Planas M d L and Ramos-Buades A 2022 *Phys. Rev. D* **105** 084040 [arXiv:2105.05872]
- [50] Hamilton E, London L, Thompson J E, Fauchon-Jones E, Hannam M, Kalaghatgi C, Khan S, Pannarale F and Vano-Vinuales A 2021 *Phys. Rev. D* **104** 124027 [arXiv:2107.08876]
- [51] Ramos-Buades A, Buonanno A, Estellés H, Khalil M, Mihaylov D P, Ossokine S, Pompili L and Shiferaw M 2023 *Phys. Rev. D* **108** 124037 [arXiv:2303.18046]
- [52] Thompson J E, Hamilton E, London L, Ghosh S, Kolitsidou P, Hoy C and Hannam M 2024 *Phys. Rev. D*

- 109** 063012 [arXiv:2312.10025]
- [53] Colleoni M, Vidal F A R, García-Quirós C, Akçay S and Bera S 2024 [arXiv:2412.16721]
 - [54] Tanay S, Haney M and Gopakumar A 2016 *Phys. Rev. D* **93** 064031 [arXiv:1602.03081]
 - [55] Moore B, Robson T, Loutrel N and Yunes N 2018 *Class. Quant. Grav.* **35** 235006 [arXiv:1807.07163]
 - [56] Moore B and Yunes N 2019 *Class. Quant. Grav.* **36** 185003 [arXiv:1903.05203]
 - [57] Hinderer T and Babak S 2017 *Phys. Rev. D* **96** 104048 [arXiv:1707.08426]
 - [58] Khalil M, Buonanno A, Steinhoff J and Vines J 2021 *Phys. Rev. D* **104** 024046 [arXiv:2104.11705]
 - [59] Ramos-Buades A, Buonanno A, Khalil M and Ossokine S 2022 *Phys. Rev. D* **105** 044035 [arXiv:2112.06952]
 - [60] Gamboa A, Khalil M and Buonanno A 2024 [arXiv:2412.12831]
 - [61] Gamboa A *et al.* 2024 [arXiv:2412.12823]
 - [62] Nagar A, Gamba R, Rettengo P, Fantini V and Bernuzzi S 2024 *Phys. Rev. D* **110** 084001 [arXiv:2404.05288]
 - [63] Liu X, Cao Z and Zhu Z H 2022 *Class. Quant. Grav.* **39** 035009 [arXiv:2102.08614]
 - [64] Liu X, Cao Z and Shao L 2023 *Int. J. Mod. Phys. D* **32** 2350015 [arXiv:2306.15277]
 - [65] Yun Q, Han W B, Zhong X and Benavides-Gallego C A 2021 *Phys. Rev. D* **103** 124053 [arXiv:2104.03789]
 - [66] Shi R, Zhou Y, Zhao T, Wang Z, Ren Z and Cao Z 2025 *Phys. Rev. D* **111** 044016 [arXiv:2411.14893]
 - [67] Joshi A V, Rosofsky S G, Haas R and Huerta E A 2023 *Phys. Rev. D* **107** 064038 [arXiv:2210.01852]
 - [68] Paul K, Maurya A, Henry Q, Sharma K, Satheesh P, Divyajyoti, Kumar P and Mishra C K 2024 [arXiv:2409.13866]
 - [69] Planas M d L, Ramos-Buades A, García-Quirós C, Estellés H, Husa S and Haney M 2025 [arXiv:2503.13062]
 - [70] Islam T, Venumadhav T, Mehta A K, Anantpurkar I, Wadekar D, Roulet J, Mushkin J, Zackay B and Zaldarriaga M 2025 [arXiv:2504.12420]
 - [71] Gayathri V, Healy J, Lange J, O’Brien B, Szczepanczyk M, Bartos I, Campanelli M, Klimentenko S, Lousto C O and O’Shaughnessy R 2022 *Nature Astron.* **6** 344–349 [arXiv:2009.05461]
 - [72] Ramos-Buades A *et al.* 2025 *In preparation*
 - [73] Ireland B, Birnholtz O, Nakano H, West E and Campanelli M 2019 *Phys. Rev. D* **100** 024015 [arXiv:1904.03443]
 - [74] Klein A 2021 [arXiv:2106.10291]
 - [75] Arredondo J N, Klein A and Yunes N 2024 *Phys. Rev. D* **110** 044044 [arXiv:2402.06804]
 - [76] Morras G, Pratten G and Schmidt P 2025 [arXiv:2502.03929]
 - [77] Phukon K S, Johnson-McDaniel N K, Singh A and Gupta A 2025 [arXiv:2504.20543]
 - [78] Liu X, Cao Z and Zhu Z H 2024 *Class. Quant. Grav.* **41** 195019 [arXiv:2310.04552]
 - [79] Gamba R, Chiamarello D and Neogi S 2024 *Phys. Rev. D* **110** 024031 [arXiv:2404.15408]
 - [80] Albanesi S, Gamba R, Bernuzzi S, Fontbuté J, Gonzalez A and Nagar A 2025 [arXiv:2503.14580]
 - [81] Romero-Shaw I M, Lasky P D, Thrane E and Bustillo J C 2020 *Astrophys. J. Lett.* **903** L5 [arXiv:2009.04771]
 - [82] Romero-Shaw I M, Lasky P D and Thrane E 2021 *Astrophys. J. Lett.* **921** L31 [arXiv:2108.01284]
 - [83] Gupte N *et al.* 2024 [arXiv:2404.14286]
 - [84] Planas M d L, Ramos-Buades A, García-Quirós C, Estellés H, Husa S and Haney M 2025 [arXiv:2504.15833]
 - [85] Morras G, Pratten G and Schmidt P 2025 [arXiv:2503.15393]
 - [86] Planas M d L, Husa S, Ramos-Buades A and Valencia J 2025 [arXiv:2506.01760]
 - [87] Gamba R, Lange J, Chiamarello D, Tissino J and Tibrewal S 2025 [arXiv:2505.21612]
 - [88] Knee A M, Romero-Shaw I M, Lasky P D, McIver J and Thrane E 2022 *Astrophys. J.* **936** 172 [arXiv:2207.14346]
 - [89] Ramos-Buades A, van de Meent M, Pfeiffer H P, Rüter H R, Scheel M A, Boyle M and Kidder L E 2022 *Phys. Rev. D* **106** 124040 [arXiv:2209.03390]
 - [90] Shaikh M A, Varma V, Pfeiffer H P, Ramos-Buades A and van de Meent M 2023 *Phys. Rev. D* **108** 104007 pypi.org/project/gw_eccentricity [arXiv:2302.11257]

- [91] Bonino A, Schmidt P and Pratten G 2024 [arXiv:2404.18875]
- [92] Boschini M, Loutrel N, Gerosa D and Fumagalli G 2025 *Phys. Rev. D* **111** 024008 [arXiv:2411.00098]
- [93] Islam T and Venumadhav T 2025 [arXiv:2502.02739]
- [94] Chartier N, Shaikh M A, Lee H M and Kim J 2025 [arXiv:2503.19538]
- [95] Schmidt P, Ohme F and Hannam M 2015 **91** 024043 [arXiv:1408.1810]
- [96] Scheel M A *et al.* 2025 [arXiv:2505.13378]
- [97] The Spectral Einstein Code <http://www.black-holes.org/SpEC.html>
- [98] SXS Collaboration The SXS collaboration catalog of gravitational waveforms <http://www.black-holes.org/waveforms>
- [99] Simulating eXtreme Spacetimes <http://www.black-holes.org/>
- [100] Mitman K *et al.* 2021 *Phys. Rev. D* **103** 024031 [arXiv:2011.01309]
- [101] Schmidt P, Hannam M, Husa S and Ajith P 2011 *Phys. Rev. D* **84** 024046 [arXiv:1012.2879]
- [102] O’Shaughnessy R, Vaishnav B, Healy J, Meeks Z and Shoemaker D 2011 *Phys. Rev. D* **84** 124002 [arXiv:1109.5224]
- [103] Boyle M, Owen R and Pfeiffer H P 2011 *Phys. Rev. D* **84** 124011 [arXiv:1110.2965]
- [104] Boyle M Scri <https://github.com/moble/scri>
- [105] Boyle M 2013 *Phys. Rev. D* **87** 104006 [arXiv:1302.2919]
- [106] Zel’dovich Y B and Polnarev A G 1974 *Sov. Astron.* **18** 17
- [107] Braginsky V B and Grishchuk L P 1985 *Sov. Phys. JETP* **62** 427–430
- [108] Braginsky V B and Thorne K S 1987 *Nature* **327** 123–125
- [109] Christodoulou D 1991 *Phys. Rev. Lett.* **67**(12) 1486–1489 <https://link.aps.org/doi/10.1103/PhysRevLett.67.1486>
- [110] Thorne K S 1992 *Phys. Rev. D* **45**(2) 520–524 <https://link.aps.org/doi/10.1103/PhysRevD.45.520>
- [111] Favata M 2010 *Class. Quant. Grav.* **27** 084036 [arXiv:1003.3486]
- [112] Mitman K *et al.* 2024 *Class. Quant. Grav.* **41** 223001 [arXiv:2405.08868]
- [113] Hokanson J M 2020 Multivariate rational approximation using a stabilized sanathanan-koerner iteration [arXiv:2009.10803] <https://arxiv.org/abs/2009.10803>
- [114] Hokanson J M polyrat <https://pypi.org/project/polyrat/> version 0.2.2
- [115] Buonanno A, Kidder L E, Mroue A H, Pfeiffer H P and Taracchini A 2011 *Phys. Rev. D* **83** 104034 [arXiv:1012.1549]
- [116] Knapp T, Chatziioannou K, Pfeiffer H, Scheel M A and Kidder L E 2025 *Phys. Rev. D* **111** 024003 [arXiv:2410.02997]
- [117] Habib S, Scheel M A and Teukolsky S A 2025 *Phys. Rev. D* **111** 084059 [arXiv:2410.05531]
- [118] Virtanen P, Gommers R, Oliphant T E, Haberland M, Reddy T, Cournapeau D, Burovski E, Peterson P, Weckesser W, Bright J, van der Walt S J, Brett M, Wilson J, Millman K J, Mayorov N, Nelson A R J, Jones E, Kern R, Larson E, Carey C J, Polat İ, Feng Y, Moore E W, VanderPlas J, Laxalde D, Perktold J, Cimrman R, Henriksen I, Quintero E A, Harris C R, Archibald A M, Ribeiro A H, Pedregosa F, van Mulbregt P and SciPy 10 Contributors 2020 *Nature Methods* **17** 261–272
- [119] Yunes N, Arun K G, Berti E and Will C M 2009 *Phys. Rev. D* **80** 084001 [Erratum: *Phys. Rev. D* 89, 109901 (2014)] [arXiv:0906.0313]
- [120] Islam T, Venumadhav T, Mehta A K, Anantpurkar I, Wadekar D, Roulet J, Mushkin J, Zackay B and Zaldarriaga M 2025 [arXiv:2504.12469]
- [121] <http://ccrg.rit.edu/~RITCatalog/>
- [122] Healy J and Lousto C O 2020 *Phys. Rev. D* **102** 104018 [arXiv:2007.07910]
- [123] Healy J and Lousto C O 2022 *Phys. Rev. D* **105** 124010 [arXiv:2202.00018]
- [124] Hinder I, Kidder L E and Pfeiffer H P 2018 *Phys. Rev. D* **98** 044015 [arXiv:1709.02007]
- [125] Savitzky A and Golay M J E 1964 *Analytical Chemistry* **36** 1627–1639 [arXiv:<https://doi.org/10.1021/ac60214a047>] <https://doi.org/10.1021/ac60214a047>
- [126] https://github.com/vijayvarma392/gw_eccentricity/blob/main/examples/gw_eccentricity_demo.ipynb